AVC-VTN-18-G03

Highly Efficient Bayesian Tomography for Multi-Phase 2-D Coda Calibration: Application to North Korea

Seung-Hoon Yoo
Weston Geophysical Corporation
181 Bedford Street, Suite 1
Lexington, MA 02420

Final Technical Report
DOS Contract SAQMMA16M2404
(September 30, 2016 – March 31, 2018)

Submitted April 11, 2018 to
U. S. Department of State
Bureau of Arms Control, Verification, and Compliance
2201 C Street, NW, Washington, DC 20520

Approved for Public Release; Distribution Unlimited

REPORT DOCUMENTATION PAGE

Form Approved
OMB No. 0704-0188

1. REPORT DATE	2. REPORT TYPE	3. DATES COVERED *(From - To)*
11/04/2018	Final Report	30/09/2016 – 31/03/2018

4. TITLE AND SUBTITLE
Highly Efficient Bayesian Tomography for Multi-Phase 2-D Coda Calibration: Application to North Korea

5a. CONTRACT NUMBER
DOS SAQMMA16M2404

5b. GRANT NUMBER

5c. PROGRAM ELEMENT NUMBER

6. AUTHOR(S)
Seung-Hoon Yoo

5d. PROJECT NUMBER

5e. TASK NUMBER

5f. WORK UNIT NUMBER

7. PERFORMING ORGANIZATION NAME(S) AND ADDRESS(ES)
Weston Geophysical Corporation
181 Bedford Street, Suite 1
Lexington, MA 02420

8. PERFORMING ORGANIZATION REPORT NUMBER

9. SPONSORING / MONITORING AGENCY NAME(S) AND ADDRESS(ES)
U.S. Department of State
Bureau of Arms Control, Verification, & Compliance
Office of Assistant Secretary / S&T Staff
2201 C Street, N.W. Washington, DC 20520

10. SPONSOR/MONITOR'S ACRONYM(S)
DOS/AVC

11. SPONSOR/MONITOR'S REPORT NUMBER(S) AVC-VTN-18-G03

12. DISTRIBUTION / AVAILABILITY STATEMENT
Approved for Public Release; Distribution Unlimited

13. SUPPLEMENTARY NOTES

14. ABSTRACT

To accomplish a full 2-D calibration capability in the coda methodology, we developed a new Bayesian calibration technique for the 2-D envelope shape correction. First, we developed a hybrid envelope template modeling technique by integrating the hybrid scattering formula, forward- and wide- angle scattering coefficients derived on 3D von Karman media, and the Markov Chain Monte–Carlo sampling method. The Bayesian interface of the template modeling technique allows us to sample the posterior distribution of the envelope shape parameters. Then, we developed a new calibration technique by adopting a trans-dimensional Bayesian tomography algorithm to map the sampled posterior of the shape parameters. In our new calibration approach, all modeling parameters for the hybrid template are physics-based and calibrated for laterally varying scattering/absorbing structures. The new hybrid envelope modeling technique includes both forward- and wide-angle- scattering effects in full-waveform 'envelope templates' that fit the direct and scattered phases in local- and regional-distance observations of low-yield explosions. The newly developed tomographic calibration technique allows us to estimate optimal envelope shape parameters for the hybrid template for given source-receiver geometry and subsequent accurate yield estimates from small local explosions. Our combined R&D development efforts are producing significantly improved fits to shorter-length signals from smaller events, as well as more accurate yield estimates. The new processing technique is also shifting conventional coda-based analysis from a strictly empirical basis to a physical one. These improvements have been long-term goals of significant interest to U.S. monitoring agencies.

15. SUBJECT TERMS
Seismic coda waves, Bayesian tomography, tomographic calibration, nuclear explosions

16. SECURITY CLASSIFICATION OF:			17. LIMITATION OF ABSTRACT	18. NUMBER OF PAGES	19a. NAME OF RESPONSIBLE PERSON
a. REPORT	b. ABSTRACT	c. THIS PAGE			Rongsong JIH (COR)
UU	UU	UU	UU	46	19b. TELEPHONE NUMBER *(include area code)* 202-647-8126

Standard Form 298 (Rev. 8-98)
Prescribed by ANSI Std. Z39.18

Table of Contents

1.0 SUMMARY 6

2.0 INTRODUCTION 6

3.0 METHODS, ASSUMPTIONS AND PROCEDURES 7

3.1 Hybrid Synthesis of Full-waveform Envelopes 7
3.2 Envelope Broadening and Scattering in von Karman Random Media 18
3.3 Exploring parameter space using Markov Chain Monte Carlo Sampling Method 24
3.4 Bayesian Tomography for 2-D Coda Calibration 28
3.4.1 Trans-Dimensional Bayesian Framework 28
3.4.2 Uncertainty in Data Noise and Hierarchical Bayes 29
3.4.3 Bayesian Mapping for the Scattering/Absorbing Parameters 30
3.4.4 Comparison between Conventional and Bayesian Tomography Techniques 31

4.0 RESULTS AND DISCUSSION 34

4.1 Application to North East Asia and North America 34
4.2 Full-Waveform Envelope Templates for Discrimination and Yield Estimation 36
4.2.2 Yield estimation of the suspected low yield event on May 12 2010 39
4.3 3-D Full-waveform Simulations for the North Korean Nuclear Tests 41

5.0 CONCLUSIONS 43

6.0 REFERENCES 44

List of Figures

Figure 1. Fig. 2 from Paasschens (1997, Physical Review E, copyright by American Physical Society). Angular average of the intensity $P(\mathbf{r},t)$ for three dimensions as a function of time t, at distance $r = 2.0l$, $2.8l$, and $4.0l$, from left to right. The solid lines are the exact result, which is very close to the interpolation formula (dashed lines). The dotted lines are the diffusion result. The intensity has a minimum for r greater than some rc..... 10

Figure 2. Modified from Figure 7 in Saito et al. (2003, copyright by the Oxford Journals). Schematic illustration of energy-packet propagation in scattering media based on the concept of the radiative-transfer theory. MS envelope can be considered as the time trace of energy density, which is composed of energy packets radiated from the source. Gray curves show energy-packet paths. The straight solid line between the source and the receiver shows the direct path. The gray curves around the direct path show multiple energy-packet paths with small angle scattering, which form the early part of the envelope, while the paths containing wide-angle scattering form coda excitation. The Markov approximation method can model multiple paths due to small-angle scattering around the direct path between a source and a receiver, as shown by the shaded area. The multiple isotropic-scattering model with momentum-transfer scattering coefficients models energy-packet paths as straight trajectories composed of isotropic scattering (dashed lines), in order to model the coda excitation. 13

Figure 3. Figure 8 in Saito *et al.* (2003, copyright by Seismological Society of America). A comparison of root-mean-square (RMS) envelopes derived from the new hybrid method (gray curves) with envelopes synthesized by the finite-difference method (solid curves) for k=0.1. 15

Figure 4. Figure 12 from Sato *et al.* (2004, copyright by American Geophysical Union). Root-mean-square (RMS) envelopes of waves for a 2-Hz Ricker wavelet source radiation in 2-D von Karman–type random media ($k = 0.1$, $\varepsilon = 0.05$, $a = 5$). The numbers above the curves indicate the distance from the source. Solid curves and thick-shaded curves show RMS envelopes based on the hybrid synthesis versus those found through finite-difference simulations, respectively. Fine-shaded curves indicate ±1 standard deviation of finite-difference envelopes. 15

Figure 5. a) semi-log and b) linear plots of the hybrid synthetic envelopes (blue lines) at 2 Hz, for von Karman-type random media ($k = 0.5$, $\varepsilon = 0.05$, $a = 5$), where k is the Hurst number, ε and a are the fractional fluctuation and characteristic length of inhomogeneity, respectively. Estimated total scattering coefficient is $8 \times 10\text{-}4\text{km-}1$ for a given random media. Green solid and red dashed lines represent the analytic solution of the radiative transfer (RT) equation and the Markov approximation of the parabolic wave equation for the random media, respectively. The Markov envelope (red dashed lines) shows the peak delay and envelope broadening with increasing travel distance, but no excitation of coda. On the other hand, the radiative transfer solution for impulsive radiation (green solid lines) models the coda excitation, but the direct arrival in the model is too impulsive, because too little energy has been forward scattered in the portion immediately after the direct arrival. The Markov and hybrid envelopes show more rapid peak amplitude decay than the RT envelope and $1/r$ geometrical spreading due to energy loss from the multiple forward scattering. 17

Figure 6. a) Scattering coefficient g(ψ) based on the Born approximation at 2 Hz in a 2-D von Karman random medium with κ =0.1. b) Comparison of the momentum transfer scattering

coefficient g_m with the scattering coefficient g(ψ) (*Sato et al.*, 2004, copyright by American Geophysical Union). 21
Figure 7. Wavenumber and frequency dependence of scattering coefficients in 3-D von Karman random media characterized by the Hurst number *k*=0.1 (a and b), *k*=0.5 (c and d), and *k*=1.0 (e and f). gπ, g0, and gmare the backward, total, momentum transfer scattering coefficients, respectively. gS0 is the scattering due to the short-scale component of the random media (Sato, 2016). 23
Figure 8. Example of the model-search using the MCMC sampling to obtain the optimal model parameters. Black solid line shows the 2-4 Hz RMS envelope and color-scaled image shows posterior distributions of predicted envelopes. Two inserted plots in each plot show posterior probability distributions of scattering and intrinsic attenuations, respectively. 25
Figure 9. Figure 6 in *Pasyanos et al.* (2012, copyright by Seismological Society of America). Waveform envelopes for the two earthquakes and two explosions recorded at Mudanjiang (MDJ) station in the 2–4 Hz passband. Synthetic envelopes for earthquakes are shown in green, with dashed and solid lines showing uncorrected and corrected synthetics, respectively. Synthetic envelopes for a 1-kt explosion at 100-m depth are shown in gray, while envelopes for the best-fitting explosions are shown in red. 26
Figure 10. Estimated characteristic time tM against distance at 2-4 Hz. Solid and dashed lines represent the best fit and ±σ. The maximum peak is delayed by ∼0.37tM seconds for 3-D propagation (spherical wavelet). 27
Figure 11. Map shows the a) scattering and b) intrinsic attenuations estimated at each station from the Mw 4.6 earthquake on 20 January 2007 shown as a black star. We will solve the posterior distributions of scattering and intrinsic attenuations using the 2-D Bayesian tomography technique to simultaneously compute 2-D attenuation models and waveform envelope shapes. 27
Figure 12. Example of Voronoi diagram, which forms a set of irregular cells that partition the plane. Any point inside a cell is closer to the node of that cell than any other node, so the shape of the parameterization is defined by the location of nodes (black dots) (wikipedia; https://en.wikipedia.org/wiki/Voronoi_diagram). 29
Figure 13. a) Synthetic model b) ray coverage for a checkerboard test. Stars, triangles and black lines represent sources, receivers, and rays between the source and receiver, respectively. 32
Figure 14. Results of the checkerboard recovery test using a) 1º×1º, b) 2º×2º, and c) 5º×5º grid spaces, respectively. Dotted and solid lines in d), e), and f) show the profile at 127.5º of synthetic and recovered models from each case. 33
Figure 15. a) Recovered model and b) estimated uncertainty of the checkerboard test using the trans-dimensional Bayesian tomography. Dotted and solid lines in c) show the profile at 127.5º of synthetic and recovered models. d) A histogram of number of cells in the Voronoi tessellation..... 33
Figure 16. a) and b) show a checkerboard recovery and uncertainty using source-receiver paths shown in e), respectively. c) and d) show tomography results and corresponding uncertainty estimates of the inelastic energy loss (Qi-1) at 1.4 Hz. 34
Figure 17. a) characteristic time, b) scattering coefficient, c) inelastic energy loss at 1 Hz..... 35
Figure 18. 1-Hz narrowband envelopes of a) a M 4.9 earthquake near California and Nevada border on 1997/11/02 08:51:54 recorded at CMB (red) and SCZ (orange), and b) a M 4.7 earthquake near Ottawa, Canada on 2013/05/17 13:43:22 recorded at WCNY (blue) and HBVT (green). Colored lines show the predicted synthetics using model parameters in Figure 6. 36

Figure 19. An example of observed full-waveform envelopes (thin gray lines) that match the new synthetic templates (green circles) for 3 September 2017 DPRK nuclear test event. Blue lines and red crosses represent the noise-corrected synthetics and template amplitudes, respectively. 37
Figure 20. Source spectrum comparison between a) earthquakes, b) 2006, 2009, 2013 DPRK tests, c) 3 September 2017 event, and d) 12 May 2010 event. Blue diamonds and red squares represent estimated source spectra using P- and S- template matching, respectively. We note that the result of the 12 May 2010 event is a single station estimate at NE3C station (~164 km)..... 38
Figure 21. Map showing the North Korean nuclear test site (star) and the seismic stations in the Dongbei Broadband Network (solid triangle) (Chun et al., 2011, copyright by the Seismological Society of America). 39
Figure 22. Vertical component waveform (left) and the narrowband envelope (right) of the observed the 2006, 2009, and 2010 events recorded at DBN08. 40
Figure 23. (left) The recovered source spectrum of the 2010 May event (blue diamond) along with the best fit of MM71 source models for the six North Korean nuclear tests (solid line). (right) The posterior distribution of yield and depth estimates from the Markov-Chain Monte Carlo inversion (blue dot) using the two assumed depths of 7m and 200m. Green and red symbols represent the posterior distribution of the estimates assuming the $122m/kt^3$ scaling and 200m fixed depth, respectively. 40
Figure 24. a) Map view of topography near the North Korean Test Site from SRTM 90-m digital elevation data (http://srtm.csi.cgiar.org) and b) an associated 3-D spectral-element mesh (40km x 40km x 20km). We used a 200-m sampling interval in the spectral-element mesh design, which is equivalent to a ~50-m grid sample size in a finite-difference modeling approach. 41
Figure 25. a) SPECFEM3D waveform synthetics observed at 10 km from a source with a 45° takeoff angle; green waveforms produced by the rough-topography simulation, black by flat-topography situation. b) The observed vertical-component velocity seismograms at the Mudanjiang (MDJ) and Ganseong (KSA) stations for the 2009 NK nuclear explosion. The behavior of the *P* and *pP* arrivals in the rough-topography synthetics matches the observed waveforms well at the MDJ and KSA azimuths. Note that the synthetic waveforms are down-going and thus have 'down' first motions. 42
Figure 26. Two-dimensional illustration of focusing/defocusing observed in depth phases generated in mountainous terrain. The elongated lens-like (or dome-like) mountain surface generates a complicated reflection of the depth phase that can be tracked azimuthally. For the example shown in Figure 3, station MDJ is to the north (enhanced *pP*) and station KSA is to the south (low-amplitude *pP*). 43

1.0 SUMMARY

Although one-dimensional (1-D) calibration of coda-based amplitude measurements has been satisfactory in simple geologic regions, its performance has been limited in regions that exhibit strong lateral variations in crustal structures (i.e. velocity, thickness, and scattering/absorbing characteristics). However, all attempts to perform two-dimensional (2-D) calibration have so far been limited to the application of 2-D attenuation corrections to coda amplitudes, and the amplitudes are still measured using simple envelope shape functions that assume a 1-D, radially symmetric Earth.

To accomplish full 2-D calibration capability in the coda methodology, we developed a new Bayesian calibration technique for the 2-D envelope shape correction. First, we developed a hybrid envelope template modeling technique by integrating the hybrid scattering formula, forward- and wide- angle scattering coefficients derived on three-dimensional (3-D) von Karman media, and the Markov Chain Monte–Carlo (MCMC) sampling method (Metropolis *et al.*, 1953; Hastings, 1970). The Bayesian interface of the template modeling technique allows us to sample the posterior distribution of the envelope shape parameters. Then, we developed a new calibration technique by adopting a trans-dimensional Bayesian tomography algorithm (Bodin *et al.*, 2009; Bodin *et al.*, 2012) to map the sampled posterior of the shape parameters.

In our new calibration approach, all modeling parameters for the hybrid template are physics-based and calibrated for laterally varying scattering/absorbing structures. The new hybrid envelope modeling technique includes both forward- and wide-angle- scattering effects (*e.g.*, Saito *et al.*, 2004) in full-waveform 'envelope templates' that fit the direct and scattered phases in local- and regional-distance observations of low-yield explosions. The newly developed tomographic calibration technique allows us to use optimal envelope shape parameters for the hybrid template for a given source-receiver geometry and calculate accurate yield estimates from small local explosions.

Our combined R&D development efforts are producing significantly improved fits to shorter-length signals from smaller events, as well as more accurate yield estimates. The new processing technique is also shifting conventional coda-based analysis from a strictly empirical basis to a physical one. These improvements have been long-term goals of significant interest to U.S. monitoring agencies.

2.0 INTRODUCTION

Seismic calibration using coda waves (*after* Mayeda and Walter, 1996) has been successful for various monitoring applications, particularly when applied to relatively large-magnitude events recorded at regional to teleseismic distances. Up to now coda yield estimations have relied on 1-D techniques that are based on a simplistic single-scattering formulation in a homogeneous medium. However, as the monitoring target extends to smaller and locally recorded events, the lower SNR and shorter length signals force us to use the earlier part of the coda, including the direct phase arrival (*e.g.*, Zhang and Wen, 2014). To remedy this problem, the current coda methodology (Mayeda *et al.*, 2003, Yoo *et al.*, 2011) must be modified to address at least two major limitations: 1) an over-simplified envelope model; and 2) a 1-D radially symmetric attenuation and code shape model.

To address the first limitation, we are currently pursuing an Air Force Research Laboratory funded project (AFRL Contract No FA9453-16-C-0022) to develop an analytic, hybrid template model that is optimized for short-duration envelopes from tamped local explosions and low-yield

explosions at regional distances (e.g., Yoo, 2017). This is a unique approach that will significantly improve upon the long-standing single-scattering methodology and, more importantly, lower magnitude thresholds and extend the methodology to smaller yield local explosions.

Despite the great success of the 1-D coda calibrations in the past, the method's performance has been limited by oversimplified parameterizations. A previous study comparing 1-D versus 2-D path corrections on coda and direct S/L_g waves using moderate-sized earthquakes in California showed that the improvement found for 2-D path corrections for coda was roughly 30% (Mayeda *et al.*, 2005). We note that this was the average improvement over all events, and we would expect even more dramatic improvement for critical paths through anomalous regions such as oceanic crust. This in turn would allow for a more accurate recovery of source spectra for those regions. For example, in the Yellow Sea/Korean Peninsula (YSKP) region, calibration for a path crossing the East Sea requires completely different velocity, coda shape, and attenuation corrections because the path is dominated by oceanic S_n propagation, whereas the bulk of the YSKP is comprised of L_g continental propagation. In fact, the recent North Korean tests illustrate this point, where we found partial blockage for paths towards the south because of short (but significant) propagation through the oceanic crust, which reduced broadband amplitudes by nearly a factor of 2 to 3 in the L_g coda. This effect was critical for yield estimation and will be equally critical in other areas of low crustal Q and L_g blockage, such as Iran. Furthermore, Mayeda *et al.* (2005) assumed the same 1-D radially symmetric envelope shape and velocity for the all stations, independent of azimuth or location. Incorporating a 2-D coda shape using our new envelope model would further reduce the variance beyond the 30% reduction observed in Mayeda *et al.* (2005).

3.0 METHODS, ASSUMPTIONS AND PROCEDURES

In this study, we conducted research and development in two stages. The first stage consisted of developing a hybrid envelope template modeling technique by integrating the hybrid scattering formula, forward- and wide- angle scattering coefficients derived on 3-D von Karman media, and the MCMC sampling method (Metropolis *et al.*, 1953; Hastings, 1970). In the second stage, we developed a new calibration technique by adopting a trans-dimensional Bayesian tomography algorithm (Bodin *et al.*, 2009; Bodin *et al.*, 2012) to map the sampled posterior of the shape parameters.

3.1 Hybrid Synthesis of Full-waveform Envelopes

A large focus of research during the first and second quarters was on developing a new forward-modeling algorithm and deriving modeling parameters that can simulate an entire waveform envelope from the direct arrival through the coda. The new algorithm is required to correctly describe the direct wavefront, the envelope broadening caused by multiple forward scattering, and the late coda caused by multiple wide-angle scattering. The algorithm needs to be fully analytic and parameterized for a physical model. It must also have a reasonable computational cost for application to a calibration approach using a massive amount of data and for application to Bayesian tomography. On the other hand, the algorithm should also have some flexibility in its formulation to allow for extra calibration of unmodeled effects (*e.g.*, site amplification, scattering conversion, and phase blockage effect etc.).

We compared previously proposed modeling techniques to determine the most suitable algorithm for our objective. To summarize, we chose a hybrid formulation originally proposed by Saito *et al.* (2003). However, we have replaced the forward-scattering term (from Markov approximation) and multiple scattering term (from Radiative Transfer Theory; RTT) in the Saito *et al.* (2003) formulation with time-domain approximate solutions (*Sato et al.*, 2012; *Paasschens*, 1997). By using time-domain solutions of the RTT and Markov approximations in our new hybrid-envelope method, we can keep the computational complexity and cost as low as that used for the single-backscattering model in the current coda calibration method (Mayeda and Walter, 1996).

Many studies we reviewed were based on 2-D random or Gaussian random media, which are far from a realistic representation of the Earth's inhomogeneity. Thus, we analytically derived all modeling parameters for a 3-D von Karman random media with a non-integer decay power. Our new forward-modeling algorithm is fully analytic and parameterized for a physical model. It allows us to simulate the multiple-phase envelope without needing prior calibration for coda-peak velocity and shape parameters. In the following section, we provide details of our new hybrid formulation.

The ensemble-averaged envelope computed from full-waveform modeling in random media is the most complete solution to the problem we are trying to solve. However, due to its high computational cost, full-waveform based methods have so far been applicable only in 2-D space. The radiative transfer theory (RTT) developed for describing energy propagation in inhomogeneous media presents a good alternative to a full-waveform modeling approach. In particular, a Monte-Carlo simulation based on RTT is a useful research tool that can model a probabilistic distribution of scattered energy density in space and time. The Monte-Carlo simulation method has been used for the synthesis of high-frequency seismograms in complex structures (*e.g.*, Hoshiba, 1994; Yoshimoto, 2000; Sanborn, 2015); however, the computational cost of the Monte-Carlo simulation is still too high to be applied in our study. We require compact, analytic solutions to the forward and inverse problems that can incorporate large numbers of events and stations.

3.1.1 Radiative Transfer Solution for Coda Excitation

Coda excitation is primarily caused by wide-angle multiple scattering due to short-wavelength spectral components of velocity inhomogeneities. An analytic solution to the conventional radiative transfer equation (RTE), describing the isotropic impulsive radiation in a homogeneous random media, can reasonably explain the coda excitation in the multiple scattering regime (*e.g.*, Sens-Schonfelder and Welger; 2006; Wegler *et al.*, 2006).

The RTE for a 3-D scattering medium characterized by the isotropic scattering coefficient g_0, and background velocity V_0, in which total energy W is spherically and impulsively radiated from a point source, is given by a convolution integral form (Sato *et al., 2012*):

$$E(\mathbb{x},t) = WG(\mathbb{x},t) + V_0 g_0 \iiint \int_{-\infty}^{\infty} G(\mathbb{x}-\mathbb{x}',t-t')E(\mathbb{x}-\mathbb{x}',t-t')\,dt'd\mathbb{x}'. \quad \text{eq. 1}$$

Here, the Green's function is given by:

$$G(\mathbb{x},t) = \frac{1}{4\pi V_0 r^2} H(t)\delta\left(t - \frac{r}{V_0}\right) e^{-(V_0 g_0 t)},$$

eq. 2

where $r = |\mathbb{x}|$.

Using this convolution integral equation (eq. 1), and taking the Fourier transform in space and the Laplace transform in time of the integral equation, we have

$$\tilde{\tilde{E}}(\mathbb{k},s) = \frac{W\tilde{\tilde{G}}(\mathbb{k},s)}{1 - V_0 g_0 \tilde{\tilde{G}}(\mathbb{k},s)}.$$

eq. 3

The local energy density $\tilde{\tilde{G}}(\mathbb{k},s)$ can be defined as an analytic form describing the conventional solution for the impulsive radiation (*e.g.*, Sato *et al., 2012*, eq. 8.24). Using the inverse Fourier-Laplace transformation, we can formally derive the space-time distribution of energy density. In practice, we can numerically evaluate the expression by substituting the inverse Fourier transform for the inverse Laplace transform (replacing s with $-i\omega$) and using a 2-D FFT (*e.g.*, Zeng, 1993; Sato *et al.*, 2012, p. 252).

As an alternative to the numerical approach, Paasschens (1997) heuristically proposed an approximate time-domain solution of the radiative transfer equation for a 3-D isotropic scattering medium (eq. 1):

$$E(r,t) \approx \frac{We^{-(V_0 g_0 t)}}{4\pi V_0 r^2}\delta\left(t - \frac{r}{V_0}\right) + W\frac{[1 - r^2/(V_0 t)^2]^{1/8}}{[4\pi V_0 t/(3g_0)]^{\frac{3}{2}}} e^{-(V_0 g_0 t)} \mathrm{M}\left[V_0 g_0 t\left(1 - \frac{r^2}{V_0^2 t^2}\right)^{\frac{3}{4}}\right] H\left(t - \frac{r}{V_0}\right),$$

eq. 4

where

$$\mathrm{M}(x) \equiv 8(3x)^{-3/2}\sum_{n=1}^{\infty}\frac{\Gamma\left(\frac{3}{4}n + \frac{3}{2}\right)}{\Gamma\left(\frac{3}{4}n\right)}\frac{x^n}{n!} \approx e^x\sqrt{1 + 2.026/x}$$

eq. 5

Figure 1 (from Fig 2 in Paasschens, 1997) shows that the difference between an exact solution of eq. 1 and its approximation is barely visible on the scale from the direct arrival to coda. The relative error of the approximation is on the order of ~2% except for the direct arrival (Paasschens, 1997). Moreover, in our hybrid envelope, we use this time-domain solution to model coda excitation by replacing the direct term in the first term of eq. 4 with the solution of

Markov approximation. Thus, the small inaccuracy issue near the ballistic peak of the approximate solution is not an issue in our hybrid formulation.

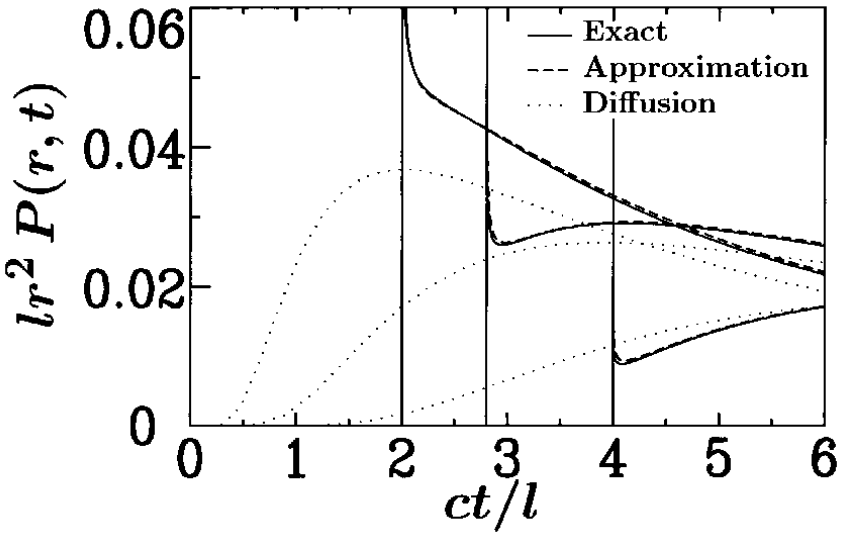

Figure 1. Fig. 2 from Paasschens (1997, Physical Review E, copyright by American Physical Society). Angular average of the intensity $P(\mathbf{r},t)$ for three dimensions as a function of time t, at distance $r = 2.0l$, $2.8l$, and $4.0l$, from left to right. The solid lines are the exact result, which is very close to the interpolation formula (dashed lines). The dotted lines are the diffusion result. The intensity has a minimum for r greater than some rc.

3.1.2 Markov Approximation for the Direct and Early coda

When the wavelength is much smaller than the correlation distance, diffraction and scattering in the forward direction dominate. In this scattering regime, we may use the parabolic wave equation, which describes wave propagation in one direction. Assuming a slowly varying harmonic wave U, propagating in z direction in an inhomogeneous media with fractional velocity fluctuation (ξ), the parabolic wave equation is given by

$$2ik_0\partial_z U + \Delta_\perp U - 2k_0^2\xi U = 0 \qquad \text{eq. 6}$$

where $\Delta_\perp \equiv \partial_x^2 + \partial_y^2$ is the Laplacian operator in the transverse plane and $k_0 = \omega/V_0$ is wavenumber. Eq.6 describes the scattering in the forward direction, neglecting backward scattering.

Next, we define the two-frequency mutual coherence function (TFMCF), Γ_2, which is the correlation of the wave field between two locations on the transverse plane ($\mathbb{x}'_\perp, \mathbb{x}''_\perp$) and two frequencies ($\omega', \omega''$) (a rigorous derivation can be found in Sato *et al.*, 2012, Chapter 9):

$$\Gamma_2(\mathbb{x}'_\perp, \mathbb{x}''_\perp, z, \omega', \omega'') = \langle U(\mathbb{x}'_\perp, z, \omega')U(\mathbb{x}''_\perp, z, \omega'')^* \rangle.$$

eq. 7

Then, the intensity spectral density (ISD) of the wavefield can be written using the inverse Fourier transform of Γ_2 with respect to angular frequency difference, $\omega_d \equiv \omega' - \omega''$:

$$\hat{I}(z,t) = \frac{1}{2\pi}\int_{-\infty}^{\infty} \Gamma_2(\mathbb{x}_{\perp d} = 0, z, \omega', \omega'') e^{-i\omega_d\left(t-\frac{z}{V_0}\right)} d\omega_d,$$

eq. 8

where $\mathbb{x}_{\perp d} = |\mathbb{x}'_{\perp} - \mathbb{x}''_{\perp}|$. This ISD describes the mean-square (MS) bandpass-filtered envelope centered at angular frequency $\omega_c \equiv (\omega' + \omega'')/2$.

Multiplying U to eq. 6 and taking the ensemble average,

$$2i\partial_z\Gamma_2 + \left(\frac{\Delta'_{\perp}}{k'_0} - \frac{\Delta''_{\perp}}{k''_0}\right)\Gamma_2 - 2\langle(k'_0\xi' - k''_0\xi')U'U''^{*}\rangle = 0$$

eq. 9

and then substituting the relation:

$$\langle(k'_0\xi' - k''_0\xi')U'U''^{*}\rangle = -\frac{i}{2}[(k'^2_0 - k''^2_0)A(0) - 2k'_0k''_0A(r_{\perp d})]\Gamma_2,$$

eq. 10

where function *A* is defined by the longitudinal integral of the autocorrelation function of random media, we have the master equation of the TFMCF:

$$2i\partial_z\Gamma_2 + \left(\frac{\Delta'_{\perp}}{k'_0} - \frac{\Delta''_{\perp}}{k''_0}\right)\Gamma_2 + i[(k'^2_0 - k''^2_0)A(0) - 2k'_0k''_0A(r_{\perp d})]\Gamma_2 = 0$$

eq. 11

Eq. 11 can be used to extrapolate the TFMCF recursively with respect to distance away from the source once the TFMCF at a slightly smaller distance is known. The term '*Markov approximation*' has its roots in the concept of a Markov process, in which the probability of future events is dependent only on most recent events (Tatarskii, 1971). The Markov approximation of the parabolic wave equation is an effective method for synthesizing the multiple forward-scattering effects caused by long-wavelength spectral components of velocity inhomogeneities (Shishov, 1974, 3-D Gaussian random media; Fehler *et al.*, 2000, 2-D Gaussian random media; Saito *et al.*, *2002*, numerical solution in 3-D von Karman random media).

The analytic forms for Γ_2 and the Markov envelope G_M without a wandering term, at a distance r, are

$$\Gamma_2(r, \theta_d, \omega_d, \omega_c) = \frac{1}{4\pi V_0}\frac{2e^{i\pi/4}\sqrt{t_M\omega_d}}{\sin\left(2e^{i\pi/4}\sqrt{t_M\omega_d}\right)}$$

and

$$G_M(r,t;\omega_c) = \frac{1}{2\pi r^2}\int_{-\infty}^{\infty}\Gamma_2(r,\theta_d,\omega_d,\omega_c)e^{-i\omega_d(t-r/V_0)}d\omega_d,$$

eq. 12

eq. 13

where t_M is the characteristic time that controls envelope and peak delay from multiple forward scattering (Fehler *et al.*, 2000; Sato *et al.*, 2012). t_M is proportional to the square of travel distance, frequency independent for Gaussian random media, and frequency dependent for a media having rich short-scale components, such as von Karman random media with $k = 0.1$. Fehler *et al.* (2000) derived the characteristic time for Gaussian random media as a simple function form, $t_M = \frac{\sqrt{\pi}\varepsilon^2 r^2}{2aV_0}$. Saito *et al.* (2002) numerically estimated the characteristic time for von Karman random media having non-integer k. Most recently, Sato (2016) derived an analytic form of the characteristic time for von Karman random media, which we use in our hybrid method. A later section will contain details about t_M in Sato (2016).

We can easily evaluate eq. 13 using the Discrete Fourier Transform (DFT) for a given t_M. However, to minimize computational complexity, we instead implemented a time-domain solution obtained by Shishov (1974):

$$G_M(r,t;\omega_c) = \frac{1}{4\pi V_0 r^2}\frac{\pi^2}{2t_M}\sum_{n=1}^{\infty}(-1)^{n+1}n^2 e^{-\frac{\pi^2 n^2}{4t_M}(t-r/V_0)}\ H\left(t-\frac{r}{V_0}\right)$$

eq. 14

using a series expansion:

$$\frac{s_0}{\sin(s_0)} = 1 + \sum_{n=1}^{\infty}\frac{(-1)^n 2{s_0}^2}{{s_0}^2 - \pi^2 n^2}.$$

eq. 15

Eq. 14 can be cast in a simplified form using an elliptic theta function of the fourth kind (see Sato *et al.*, 2012, p 351):

$$\vartheta_4(v,q) = 1 + \sum_{n=1}^{\infty}(-1)^n q^{n^2}\cos 2nv,$$

eq. 16

leading to

$$G_M(r,t;\omega_c) = \frac{1}{4\pi V_0 r^2}\frac{\pi^2}{16t_M}\vartheta_4''\left(0, e^{-\frac{\pi^2}{4t_M}(t-r/V_0)}\right)\ H\left(t-\frac{r}{V_0}\right),$$

eq. 17

where ϑ_4'' is the second derivative of elliptic theta function of the fourth kind with respect to v. The infinite series sum in the elliptic theta function converses very quickly due to exponential decay in time. Thus, eq. 17 has a much lower computation cost compared to eq. 13. Moreover, we only need to compute the Markov envelope once in practice, because the Markov envelope is scalable by t_M. By using time-domain solutions of RTT and Markov approximation in our hybrid envelope, we are able to keep the computational complexity and cost the same as the single-backscattering model in the current coda calibration method (Mayeda and Walter, 1996).

3.1.3 Hybrid Formulation

Figure 2 shows a schematic illustration of energy-packet propagation in a scattering medium based on the concept of RTT. For smooth random media, small-angle scattering around the forward direction is dominant. The Markov approximation method, which correctly accounts for multiple-forward scattering and disregards wide-angle scattering, reliably models propagation around the direct path. On the other hand, for rough random media, the short-wavelength components of inhomogeneity efficiently excite wide-angle scattering. In this situation scattered waves distributed far from the direct path contribute to the excitation of coda waves.

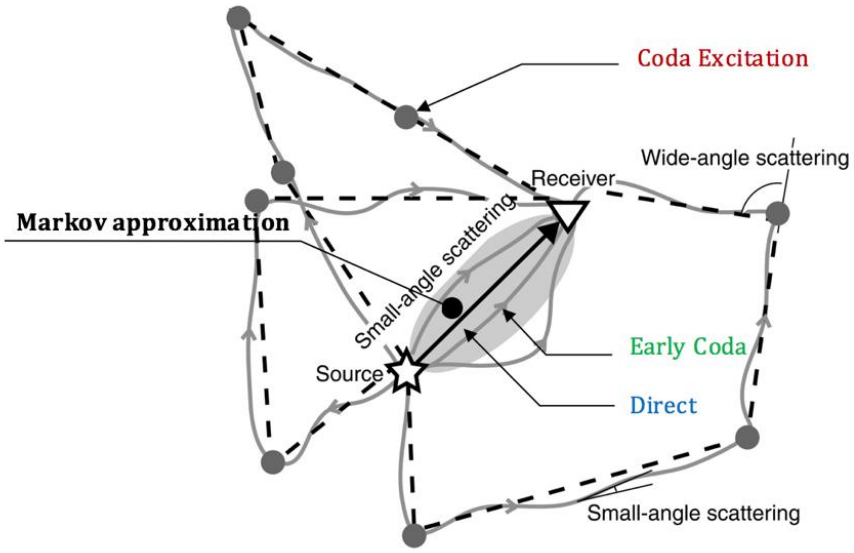

Figure 2. Modified from Figure 7 in Saito et al. (2003, copyright by the Oxford Journals). Schematic illustration of energy-packet propagation in scattering media based on the concept of the radiative-transfer theory. MS envelope can be considered as the time trace of energy density, which is composed of energy packets radiated from the source. Gray curves show energy-packet paths. The straight solid line between the source and the receiver shows the direct path. The gray curves around the direct path show multiple energy-packet paths with small angle scattering, which form the early part of the envelope, while the paths containing wide-angle scattering form coda excitation. The Markov approximation method can model multiple paths due to small-angle scattering around the direct path between a source and a receiver, as shown by the shaded area. The multiple isotropic-scattering model with momentum-transfer scattering coefficients models energy-packet paths as straight trajectories composed of isotropic scattering (dashed lines), in order to model the coda excitation.

The initial pulse in RTT-derived envelopes are too impulsive due to the use of the delta function propagator in the RTE (see green curves in Figure 5). Ultimately, the RTT solution fails to explain the envelope near the direct arrival because it neglects the narrow-angle scattering around the forward direction near the direct arrivals. On the other hand, assumption of the parabolic wave equation neglects the wide-angle scattering and the coda excitation is not modeled in the Markov approximation (see red dotted curves in Figure 5).

In order to model the coda excitation due to wide-angle scattering and envelope broadening due to multiple forward scattering, Saito *et al.* (2003) first proposed to replace the direct propagation term of the RTE solution with the solution of the Markov approximation envelope for the direct propagation:

$$E(r,t;\omega_c) = WG_M(r,t;\omega_c) + E^1(r,t;\omega_c) + E^M(r,t;\omega_c)$$

eq. 18

where E^1 and E^M are a single- and multiple-scattering energy envelopes, respectively.

The propagator used in the RTE solution (Saito *et al.*, 2003) was still a delta function-type,), and thus Sato *et al.* (2004) proposed an improved hybrid method that utilized the Markov approximation as a propagator in the radiative transfer integral equation:

$$\tilde{\hat{E}}(\mathbb{k},s) = \frac{W\widetilde{\widehat{G_M}}(\mathbb{k},s)}{1 - V_0 g_0 \widetilde{\widehat{G}_M}(\mathbb{k},s)}.$$

eq. 19

We note that, in a similar fashion as with eq. 3, we can solve eq. 19 using the 2-D FFT technique.

Figures 3 and 4 show comparisons between the two hybrid envelopes of Saito *et al.* (2003) and Sato *et al.* (2004) in a 2-D von Karman random media ($k = 0.1$, $\varepsilon = 0.05$, $a = 5$), with an envelope synthesized using the finite-difference method. The results show that the envelopes computed with the hybrid methods agree well with envelopes averaged over an ensemble of finite-difference simulations of the wave equation for a suite of random media. More interestingly, the simple hybrid method proposed by *Saito et al.* (2003) explains both the envelope broadening around the peak and the coda excitation with a far lower computational cost.

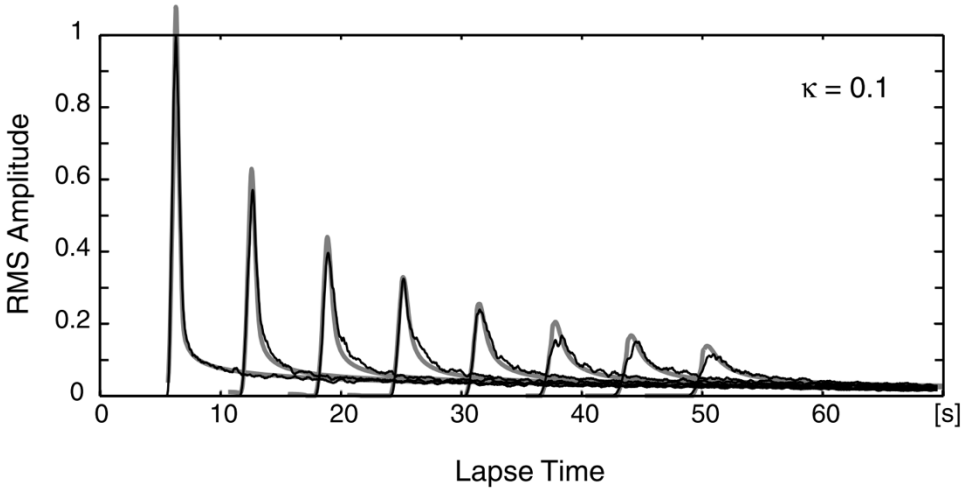

Figure 3. Figure 8 in Saito *et al.* (2003, copyright by Seismological Society of America). A comparison of root-mean-square (RMS) envelopes derived from the new hybrid method (gray curves) with envelopes synthesized by the finite-difference method (solid curves) for k=0.1.

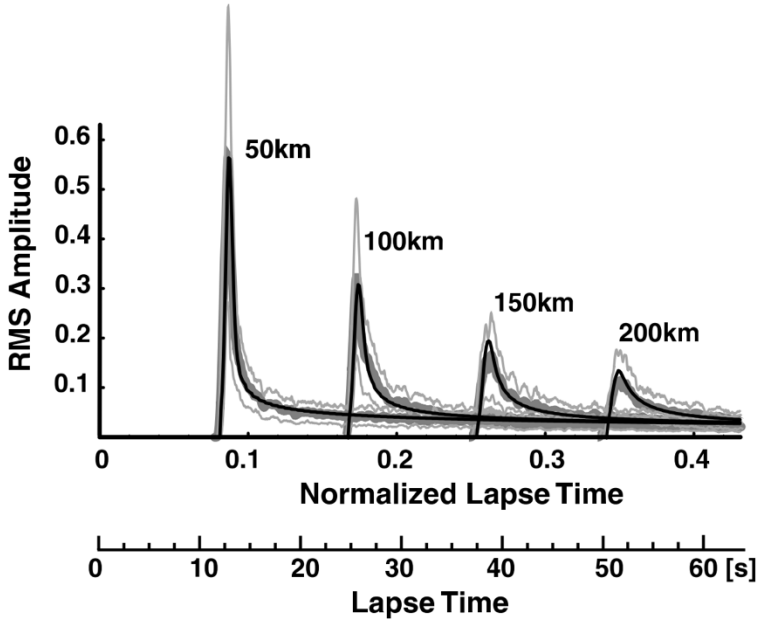

Figure 4. Figure 12 from Sato *et al.* (2004, copyright by American Geophysical Union). Root-mean-square (RMS) envelopes of waves for a 2-Hz Ricker wavelet source radiation in 2-D von Karman–type random media ($k = 0.1$, $\varepsilon = 0.05$, $a = 5$). The numbers above the curves indicate the distance from the source. Solid curves and thick-shaded curves show RMS envelopes based on the hybrid synthesis versus those found through finite-difference simulations, respectively. Fine-shaded curves indicate ±1 standard deviation of finite-difference envelopes.

For our template modeling, we chose the hybrid approach proposed by Saito *et al.* (2003) because of its computational simplicity. The hybrid method by proposed Sato *et al.* (2004) requires computation of the Markov approximation kernel in time and space, as well as a 2-D Fourier-Laplace transform for the convolution integral equation. It therefore has a much higher

computational complexity and cost compared to the method in Saito *et al.* (2003). We can also accelerate the calculation using an approximate analytic time-domain solution (e.g., RT solution for Paasschens, 1997; time-domain solution of the Markov approximation for Sato *et al.*, 2012).

Replacing the first term in the 3-D radiative-transfer solution (eq. 4) with the Markov envelope (eq. 17), and including a scattering energy loss term $e^{-(V_0 g_{S0} t)}$, we derive a 3-D hybrid envelope:

$$E(r,t) = \frac{1}{4\pi V_0 r^2}\frac{\pi^2}{16 t_M}\vartheta_4''\left(0, e^{-\frac{\pi^2}{4t_M}(t-r/V_0)}\right) e^{-(V_0 g_{S0} t)} H\left(t-\frac{r}{V_0}\right) + W\frac{[1-r^2/(V_0 t)^2]^{1/8}}{[4\pi V_0 t/(3g_m)]^{\frac{3}{2}}} e^{-(V_0 g_m t)} \mathrm{M}\left[V_0 g_m t\left(1-\frac{r^2}{V_0^2 t^2}\right)^{\frac{3}{4}}\right] H\left(t-\frac{r}{V_0}\right),$$

eq. 20

Based on eq. 20, the bandpass filtered velocity envelope centered at frequency f at a distance r can be calculated by

$$A(r,t,f;t_M,g_0,b) = [2\rho_0^{-1} S(f) P(f) E(r,t,f;t_M,g_0) e^{-bt} + N^2(f)]^{1/2}$$

eq. 21

where S, P and N are respectively the source, frequency dependent site effect, and noise spectra, and b is the intrinsic attenuation factor ($b \equiv \frac{2\pi f}{Q_i}$) and ρ_0 is density. Doubling the energy density accounts for the boundary condition for energy transfer in a half-space (*c.f.*, Sens-Schonfelder and Wegler, 2006).

Figure 5 illustrates some results for a 3-D von Karman-type random media. We show envelopes computed using the hybrid method compared to those computed using the analytic solution of the radiative transfer equation and the Markov approximation of parabolic wave equation.

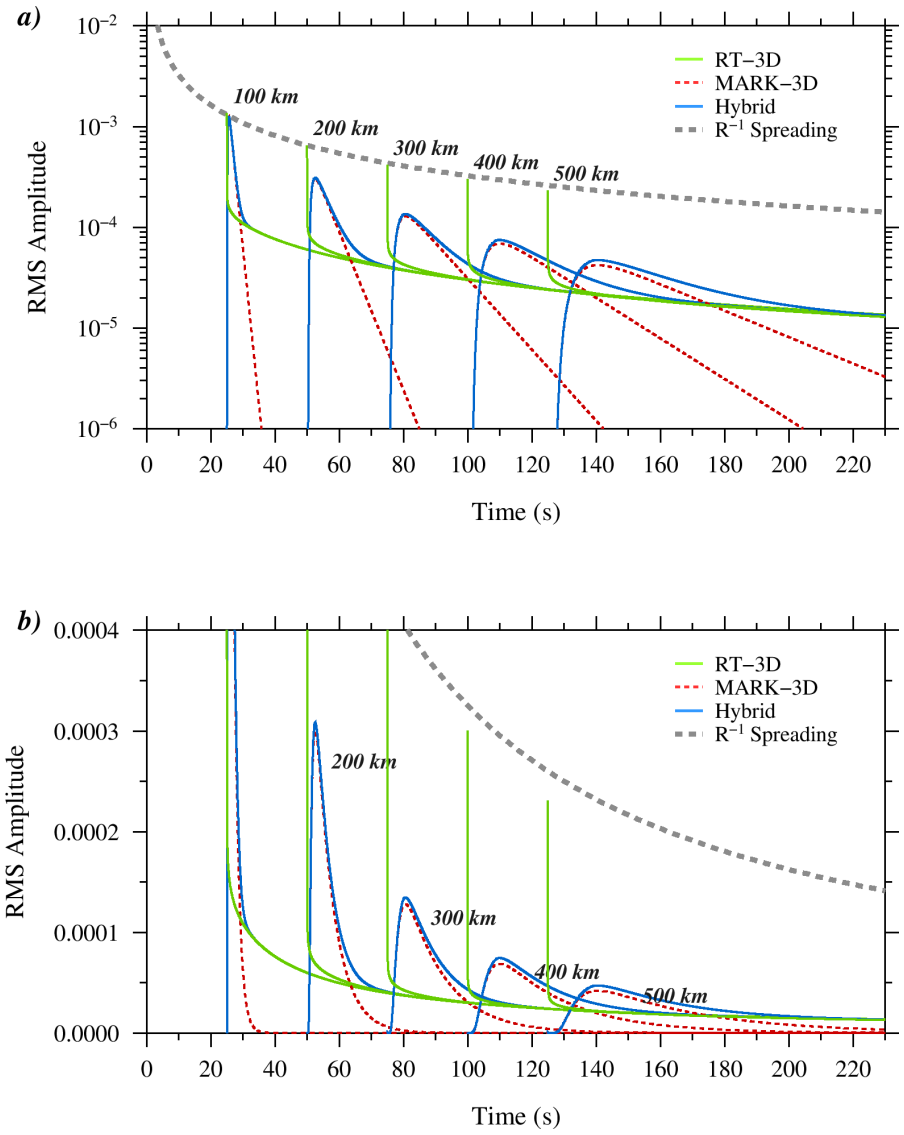

Figure 5. a) semi-log and b) linear plots of the hybrid synthetic envelopes (blue lines) at 2 Hz, for von Karman-type random media ($k = 0.5$, $\varepsilon = 0.05$, $a = 5$), where k is the Hurst number, ε and a are the fractional fluctuation and characteristic length of inhomogeneity, respectively. Estimated total scattering coefficient is $8 \times 10^{-4} km^{-1}$ for a given random media. Green solid and red dashed lines represent the analytic solution of the radiative transfer (RT) equation and the Markov approximation of the parabolic wave equation for the random media, respectively. The Markov envelope (red dashed lines) shows the peak delay and envelope broadening with increasing travel distance, but no excitation of coda. On the other hand, the radiative transfer solution for impulsive radiation (green solid lines) models the coda excitation, but the direct arrival in the model is too impulsive, because too little energy has been forward scattered in the portion immediately after the direct arrival. The Markov and hybrid envelopes show more rapid peak amplitude decay than the RT envelope and $1/r$ geometrical spreading due to energy loss from the multiple forward scattering.

3.2 Envelope Broadening and Scattering in von Karman Random Media

Sonic well-logging data show that velocity inhomogeneities are random and their power spectral density function (PSDF) decreases with some negative power of wavenumber. Von Karman-type random media have power-law spectra at large wavenumbers, so they are often used for describing Earth's inhomogeneity. The autocorrelation function (ACF) of a von Karman random media characterized by correlation distance (a) and fractional fluctuation (ε) is given by

$$R(\mathbb{x}) = R(r) = \frac{\varepsilon^2 2^{1-k}}{\Gamma(k)} \left(\frac{r}{a}\right)^k K_k\left(\frac{r}{a}\right) \qquad \text{for } k = 0{\sim}1,$$

eq. 22

where $\Gamma(k)$ is the gamma function and K_k is the modified Bessel function of the second kind of order k. For the 3-D case, the PSDF is

$$P(\mathbb{m}) = P(m) = \frac{8\pi^{3/2}\Gamma(k+3/2)\varepsilon^2 a^3}{\Gamma(k)(1+a^2m^2)^{k+3/2}},$$

eq. 23

where $\mathbb{m}$ is the wavenumber vector and $m = |\mathbb{m}|$. The PSDF obeys a power law for large wavenumbers ($am \gg 1$), where the decay rate is controlled by the Hurst number, k. The von Karman random media is rich in short wavelength components compared with that of Gaussian-type random media. The von Karman random media with $k = 0.5$ is an exponential random media.

Saito *et al.* (2002) numerically solved the master equation of TFMCF (eq. 13) for a von Karman random media having non-integer k. Most recently, Sato (2016) solved the equation fully analytically by decomposing the random velocity fluctuation into two components: the low-wavenumber spectral component and the high-wavenumber spectral component.

As a simple mathematical model, Sato (2016) proposed a new stochastic synthesis of the scalar wavelet envelope in 3-D von Karman-type random media, for the case when the center wavenumber of the wavelet ($k_c = \omega_c/V_0$) is higher than the corner wavenumber (a^{-1}) of the PSDF. The key idea is to split the random medium spectrum into two components using the center wavenumber as a reference: the long-scale (P_L; low-wavenumber spectral) component produces the peak delay and the envelope broadening by multiple scattering around the forward direction; the short-scale (P_S; high-wavenumber spectral) component attenuates wave amplitude by wide-angle scattering:

$$P(\mathbb{m}) = P_L(\mathbb{m}) + P_S(\mathbb{m}).$$

eq. 24

Sato (2016) took the corner wavenumber of the PSDF of the short-scale component as

$$a_S^{-1} = \zeta k_c,$$

eq. 25

where $k_c(=\omega_c/V_0)$ is the center wavenumber and ζ is a precise tuning parameter of the order of one. He defined the parameter ν in the following equation:

$$\nu \equiv \frac{a_S^{-1}}{a^{-1}} = \zeta a k_c.$$

eq. 26

From eq. 23, eq. 25 and eq. 26, the PSDF of the short scale component of random media (P_S) is

$$P_S(m) \equiv \frac{8\pi^{\frac{3}{2}}\Gamma\left(k+\frac{3}{2}\right)\varepsilon_S^2 a_S^3}{\Gamma(k)(1+a_S^2m^2)^{k+\frac{3}{2}}} = \frac{8\pi^{\frac{3}{2}}\Gamma\left(k+\frac{3}{2}\right)\varepsilon^2 a^3}{\Gamma(k)(\nu^2+a^2m^2)^{k+\frac{3}{2}}}$$

$$= \frac{8\pi^{3/2}\Gamma(k+3/2)\varepsilon^2 a^3}{\Gamma(k)((\zeta a k_c)^2+a^2m^2)^{k+3/2}}.$$

eq. 27

3.2.1 Envelope Broadening and Peak Delay due to the Long-Scale Component in von Karman Random Media

The time width of an envelope is well characterized by the characteristic time, t_M. By decomposing a random medium into two components, Sato (2016) analytically derived the characteristic time for the long-scale (low-wavenumber spectral) component of 3-D von Karman type random media (P_L):

$$t_M(k,\xi,k_c,r_0) = \frac{\varepsilon^2}{2v_0 a} C_L(k,\xi,k_c) r_0^2,$$

eq. 28

where

$$C_L(k,\xi,k_c) = \begin{cases} \frac{\sqrt{\pi}\Gamma\left(k+\frac{1}{2}\right)}{(2k-1)\Gamma(k)}\left[1-(\zeta a k_c)^{1-2k}\right] & \text{for } k \neq \frac{1}{2} \\ \ln \zeta k_c & \text{for } k = \frac{1}{2} \end{cases}.$$

eq. 29

As we see from the equations, t_M is proportional to the square of travel distance and frequency dependent as a function of wavenumber. The frequency dependency increases for rougher media with lower k. For 3-D von Karman random media, we found that the delay time between the onset and the peak arrival is $\sim 0.37 t_M$.

3.2.2 Attenuation Correction for the Markov Approximation due to the Short-Scale Component in von Karman Random Media

The Markov envelope with characteristic time t_M simulates the envelope broadening effect by multiple scattering in a narrow cone around the forward direction, due to the long-scale component of random media. This approximation ignores attenuation due to wide angle scattering that is caused by the short-scale component of random media.

Sato (2016) proposed to use the total scattering coefficient derived using the short-scale component of random media P_S as the lowest correction to the Markov envelope for scattering attenuation by wide angle. We note that Saito *et al.* (2003) numerically estimated this effect.

The scattering coefficient defined as the scattering power per unit volume is directly related to the PSDF of the velocity fractional fluctuation. For the 3-D case, the scattering coefficient for the angular frequency (ω) and scattering angle (ψ) is given by (Sato *et al.*, 2012, eq. (4.25)):

$$g(\psi;\omega) \equiv 4\pi \frac{1}{L^3}\left\langle \frac{d\sigma}{d\Omega} \right\rangle = \frac{k_0^4}{\pi} P\left(2k_0 \sin\frac{\psi}{2}\right),$$

eq. 30

where $k_0$is wavenumber (ω/V_0). The total scattering coefficient is given by the solid angle average:

$$\begin{aligned} g_0(\omega) &= \frac{1}{4\pi}\oint g(\psi;\omega)\, d\Omega(\psi,\omega) \\ &= \frac{1}{2}\int_0^{\pi} g(\psi;\omega)\sin\psi\, d\psi \\ &= \frac{k_0^4}{2\pi}\int_0^{\pi} P\left(2k_0 \sin\frac{\psi}{2}\right)\sin\psi\, d\psi \\ &= \frac{k_0^2}{2\pi}\int_0^{2k_0} P(m)\, m\, dm \end{aligned}$$

eq. 31

The total scattering coefficient of the short-scale component is derived from eq. 27 and eq. 31

$$g_{S0}(k,\zeta,k_0) = \frac{\varepsilon^2}{a}\frac{2\pi^{1/2}\Gamma(k+1/2)}{\Gamma(k)}\left[1-\frac{1}{(1+4\zeta^{-2})^{k+1/2}}\right]\frac{(\zeta a k_0)^{1-2k}}{\zeta^2}$$

eq. 32

3.2.3 Scattering Coefficients for the Coda Excitation

Another important quantity in radiative transfer theory is the transport scattering coefficient, which is also called the momentum transfer scattering coefficient (Morse and Feshbach, 1953). Even though the scattering is anisotropic, the scattering process can be well described by isotropic scattering when the multiple scattering process is dominant. The transport scattering

coefficient is defined by adding an additional factor $(1-\cos\psi)$ to exclude forward scattering to the total scattering coefficient eq. 34:

$$
\begin{aligned}
g_m(\omega) &= \frac{1}{4\pi}\oint g(\psi;\omega)(1-\cos\psi)d\Omega(\psi,\omega) \\
&= \frac{1}{2}\int_0^{\pi} g(\psi;\omega)(1-\cos\psi)\sin\psi\, d\psi \\
&= \frac{k_0^4}{2\pi}\int_0^{\pi} P\left(2k_0\sin\frac{\psi}{2}\right)(1-\cos\psi)\sin\psi\, d\psi \\
&= \frac{1}{4\pi}\int_0^{2k_0} P(m)m^3 dm
\end{aligned}
$$

eq. 33

The factor $(1-\cos\psi)$ also works as a filter that eliminates the long-scale component of the spectra of the random media (Figure 6). Thus, the transport scattering coefficient can be interpreted as the effective isotropic scattering in the multiple scattering regime, which is the average contribution of wide-angle scattering.

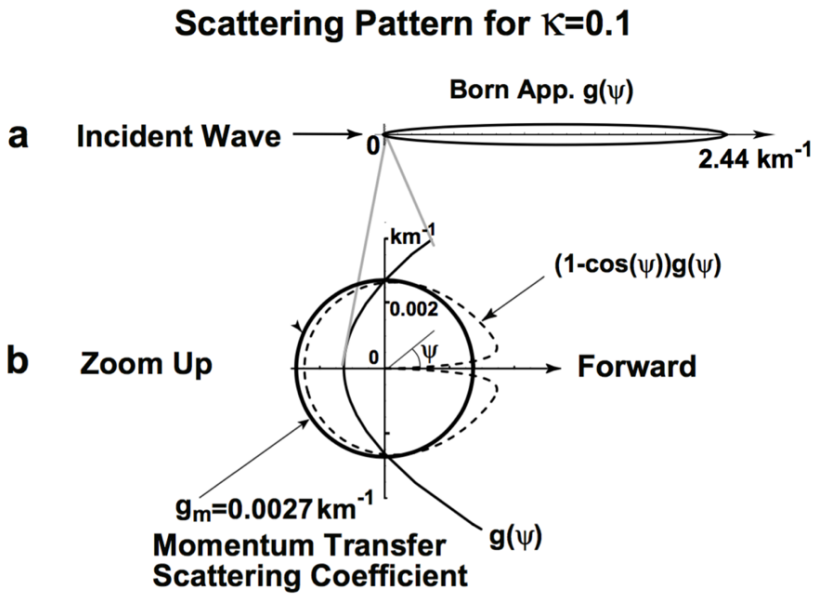

Figure 6. a) Scattering coefficient g(ψ) based on the Born approximation at 2 Hz in a 2-D von Karman random medium with κ =0.1. b) Comparison of the momentum transfer scattering coefficient g_m with the scattering coefficient g(ψ) (*Sato et al.*, 2004, copyright by American Geophysical Union).

We derived the analytic form of the moment transfer scattering coefficient for a 3-D von Karman random media having non-integer k from eq. 23 and eq. 33:

$$g_m(k,\zeta,k_0) = \frac{\varepsilon^2}{a}\frac{2\pi^{1/2}\Gamma(k+1/2)}{(2k-1)\Gamma(k)}\left[1-\frac{1+2a^2k_0^2(2k+1)}{(1+4a^2k_0^2)^{k+\frac{1}{2}}}\right],$$

eq. 34

and for the exponential random media ($k = 0.5$),

$$g_m(k,\zeta,k_0) = \frac{\varepsilon^2}{a}\left[\ln(1+4a^2k_0^2) - \frac{4a^2k_0^2}{1+4a^2k_0^2}\right].$$

eq. 35

For comparison, we also derived the total scattering coefficient from eq. 23 and eq. 31 and a backscattering coefficient ($g_\pi \equiv g(\psi = \pi)$).

$$g_0(k,\zeta,k_0) = \varepsilon^2 a k_0^2 \frac{2\pi^{1/2}\Gamma(k+1/2)}{\Gamma(k)}\left[1-\frac{1}{(1+4a^2k_0^2)^{k+1/2}}\right]$$

eq. 36

$$g_\pi(k,\zeta,k_0) = \frac{8\pi^{1/2}\Gamma(k+3/2)}{\Gamma(k)}\frac{\varepsilon^2 a^3 k_0^4}{(1+4a^2k_0^2)^{k+3/2}}$$

eq. 37

Figure 7 shows wavenumber and frequency dependence of the scattering coefficients for 3-D von Karman random media. The wavenumber and frequency dependence of the transport scattering become stronger for a rough media (e.g., $k < 0.5$). We note that the scattering attenuation effect (g_{S0}) in the Markov solution due to the short scaling component of random media is also important for the rough media.

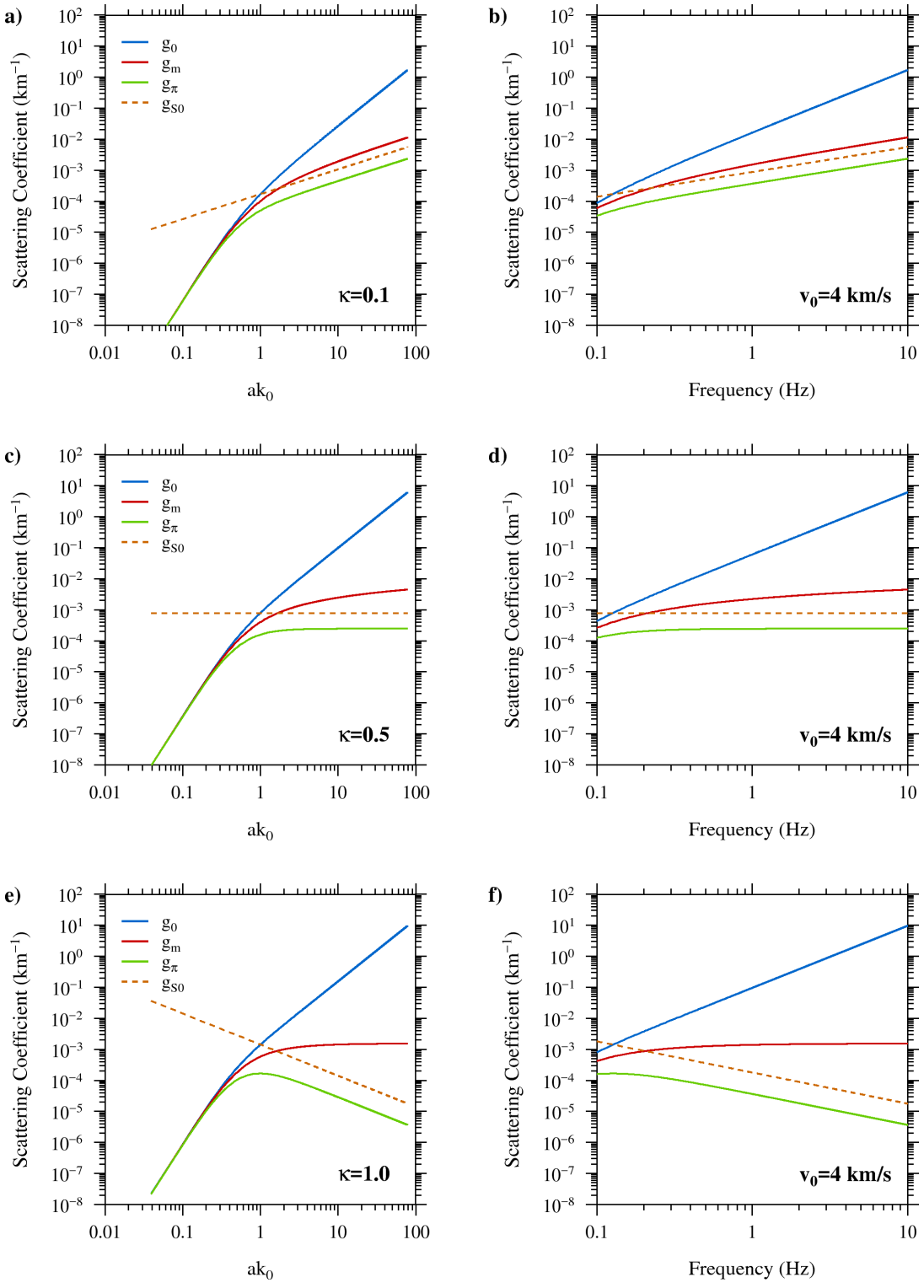

Figure 7. Wavenumber and frequency dependence of scattering coefficients in 3-D von Karman random media characterized by the Hurst number k=0.1 (a and b), k=0.5 (c and d), and k=1.0 (e and f). g_π, g_0, and $g_m$are the backward, total, momentum transfer scattering coefficients, respectively. g_{S0} is the scattering due to the short-scale component of the random media (Sato, 2016).

3.3 Exploring parameter space using Markov Chain Monte Carlo Sampling Method

We have completed the hybrid envelope modeling technique by integrating the hybrid scattering formula, forward- and wide- angle scattering coefficients derived on 3D von Karman media, and the MCMC sampling method (Metropolis *et al.*, 1953; Hastings, 1970). Using the modeling code, we explored the model parameter space of the new forward modeling by matching the observed envelope recorded at local and regional distances. This step validated the new forward modeling and examined the sensitivity of each model parameter.

We explored the modeling parameters control on the shape and attenuation of the crustal phases' envelopes (P_g and L_g). In this new formulation, all modeling parameters that control the forward and wide-angle scatterings were consistently derived for a 3-D von Karman random media. For validation purpose, we chose the same dataset we studied using the L_g-coda calibration method (Yoo *et al.*, 2010). The dataset includes 409 earthquakes recorded at 25 broadband stations in Korean Peninsula.

In this test, we solved the P_g and L_g templates separately, assuming no scattering conversion. Also, we only fit a single frequency band, 2-4 Hz, and we directly sampled the source amplitude rather than sampling the seismic moment and corner frequency in this test. The source estimates still include the site amplification in the current test as we didn't sample the site term in the MCMC model search.

For this test, first we assume that the misfit is distributed normally with zero mean and some known variance, σ^2. We then express the log-likelihood function for envelope model,

$$l(a, \varepsilon, k, Q_0, \eta, S) = \log\left[\prod_i^{NT\times NF} \frac{1}{\sqrt{2\pi\sigma^2}} \exp\left(-\frac{[\log_{10} A(r,t,f;a,\varepsilon,k,Q_0,\eta,S) - \log_{10} D(r,t,f)]^2}{2\sigma^2}\right)\right]$$

eq. 38

where A is a model prediction proposed by parameters $a, \varepsilon, k, Q_0, \eta, S$ using eq. 23 and D is the observed RMS envelope defined as a vector sum of the three component velocity seismogram ($u_{N,E,Z}$),

$$D(t,f) = [u_N^2 + u_E^2 + u_Z^2]^{\frac{1}{2}}$$

eq. 39

For each observation, we proposed a total of 2 million sets of models (1 million for a burn-in process and another 1 million for a model sampling), sampled 1,000 sets from the 1 million and obtained a distribution of the predicted envelope models and model parameters. From the set of predicted model parameters, we computed the distribution of scattering and intrinsic attenuations,

$$Q_S^{-1} = \frac{v g_0}{2\pi f} \text{ and } Q_i^{-1} = (Q_0 f^{\eta})^{-1}.$$

eq. 40

Figure 8 show the 2-4 Hz RMS envelopes at 2-4 Hz and predicted models for a Mw 4.6 earthquake that occurred in the mid-east Korea Peninsula on 20 January 2007. Our new hybrid model fits the data very well, showing a large improvement on fit compared to the previous coda model (see Figure 9 from Pasyanos *et al.*, 2012). The simple exponential coda model seems to work reasonably well for the later arrival of S-coda, but their model fails to predict the entire P-coda envelopes and earlier part of S-coda as well. The simple exponential coda model is originally designed for S-coda after roughly twice the travel time of an S-wave.

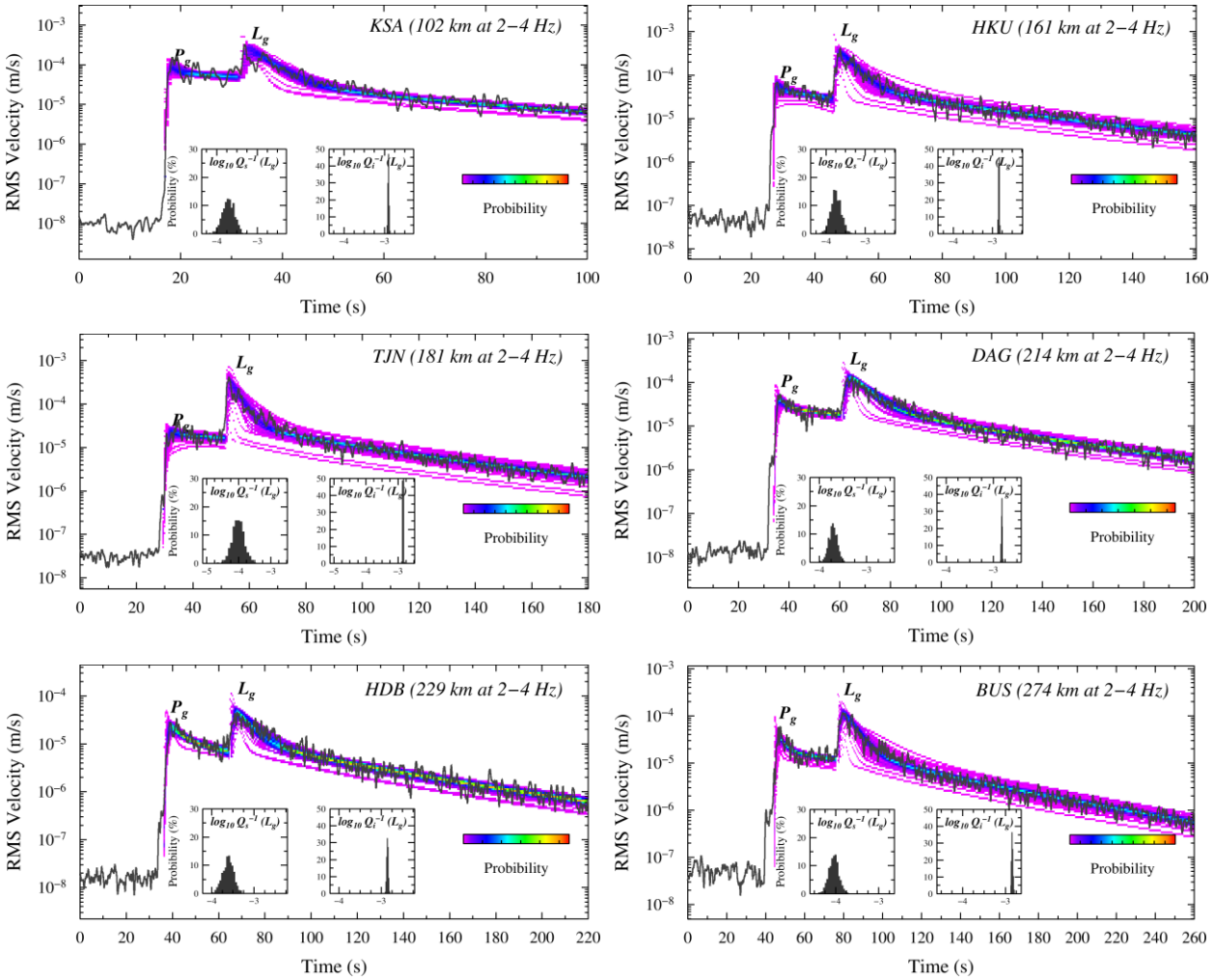

Figure 8. Example of the model-search using the MCMC sampling to obtain the optimal model parameters. Black solid line shows the 2-4 Hz RMS envelope and color-scaled image shows posterior distributions of predicted envelopes. Two inserted plots in each plot show posterior probability distributions of scattering and intrinsic attenuations, respectively.

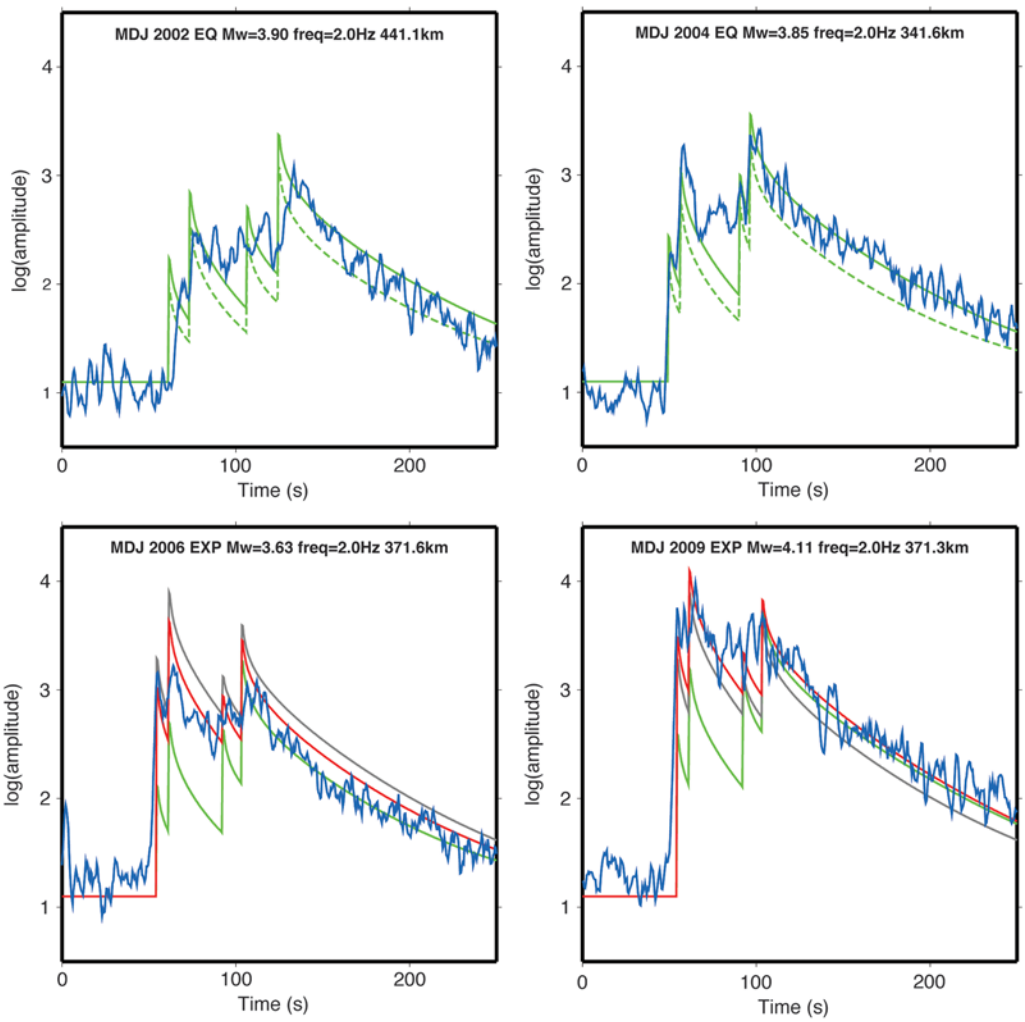

Figure 9. Figure 6 in *Pasyanos et al.* (2012, copyright by Seismological Society of America). Waveform envelopes for the two earthquakes and two explosions recorded at Mudanjiang (MDJ) station in the 2–4 Hz passband. Synthetic envelopes for earthquakes are shown in green, with dashed and solid lines showing uncorrected and corrected synthetics, respectively. Synthetic envelopes for a 1-kt explosion at 100-m depth are shown in gray, while envelopes for the best-fitting explosions are shown in red.

Figures 10 shows that estimated characteristic time t_M increases with distance. This parameter controls envelope broadening and peak delay due to the multiple forward scattering. The maximum peak arrival is delayed by $\sim 0.37 t_M$ seconds for 3-D propagation (spherical wavelet).

Figure 11 shows a spatial distribution of the estimated scattering and intrinsic attenuation. The estimated scattering attenuation is smaller almost by order of magnitude than the intrinsic attenuation which indicated that intrinsic absorption is a dominant contributor to the high frequency attenuation process in the Korea Peninsula. This observation agrees well with previous studies using the Multi-Lapse Time Windows Analysis based on the Monte-Carlo simulation method (Chung *et al.*, 2010).

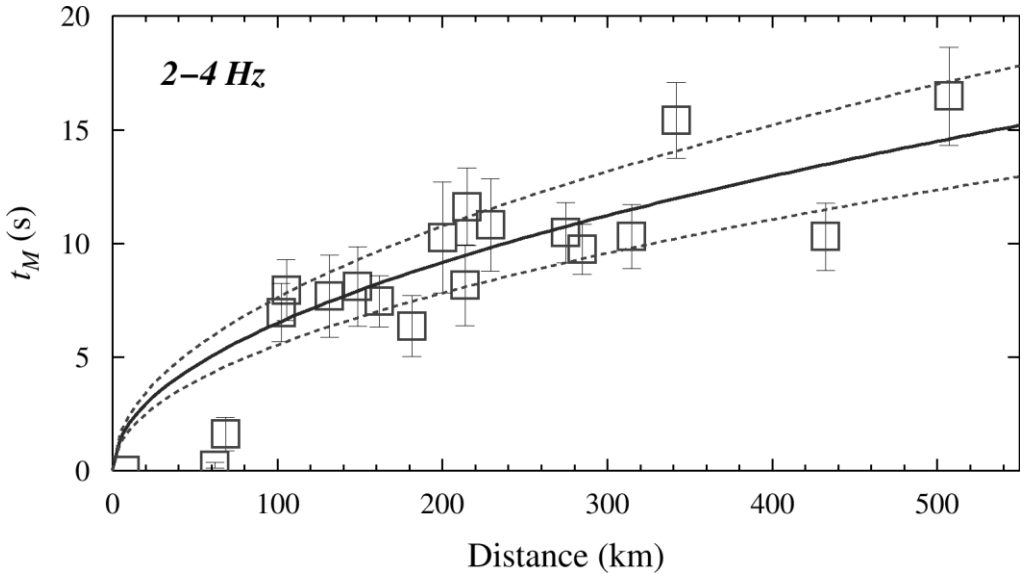

Figure 10. Estimated characteristic time t_M against distance at 2-4 Hz. Solid and dashed lines represent the best fit and ±σ. The maximum peak is delayed by $\sim 0.37 t_M$ seconds for 3-D propagation (spherical wavelet).

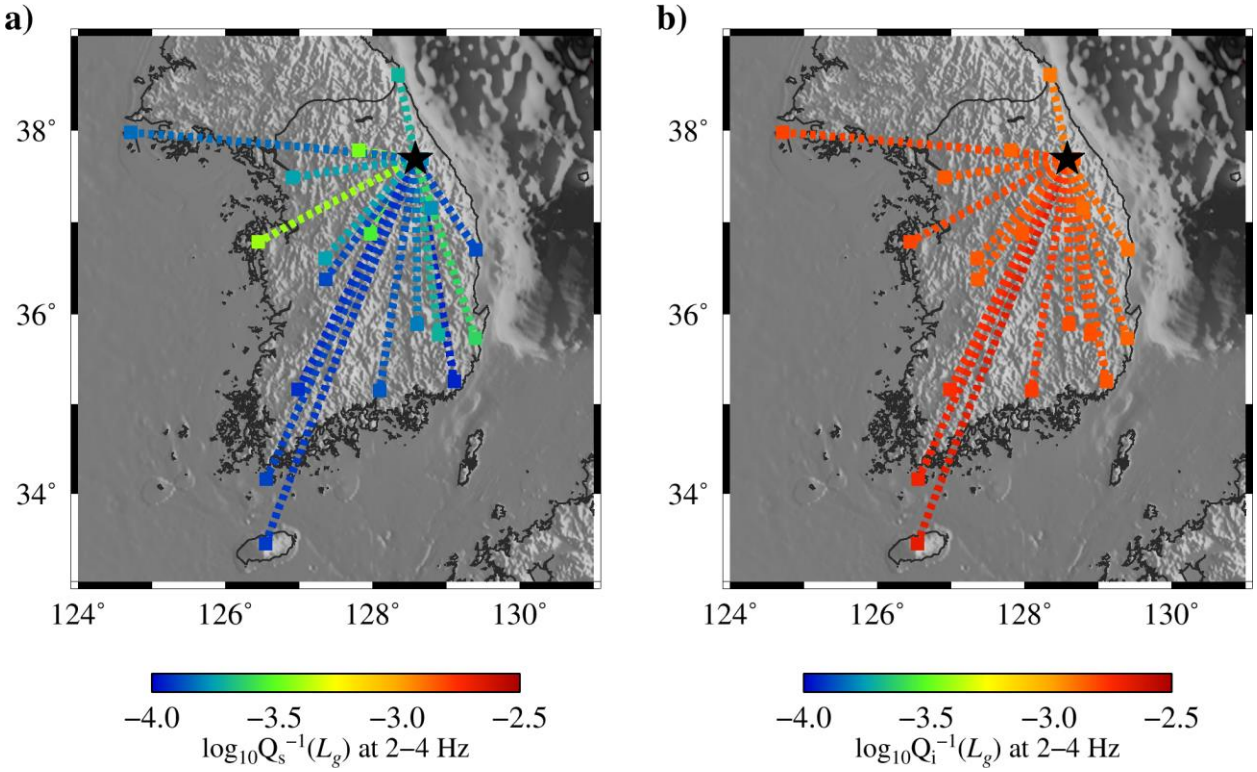

Figure 11. Map shows the a) scattering and b) intrinsic attenuations estimated at each station from the Mw 4.6 earthquake on 20 January 2007 shown as a black star. We will solve the posterior distributions of scattering and intrinsic attenuations using the 2-D Bayesian tomography technique to simultaneously compute 2-D attenuation models and waveform envelope shapes.

As we found from the test data, the characteristic time, scattering and intrinsic attenuations coefficients are well separated and constrained by the MCMC approach using the new hybrid model provides excellent fits to entire envelope for both crustal phases. The posterior probability distributions of these parameters will be used as input data for the 2-D Bayesian tomography later.

3.4 Bayesian Tomography for 2-D Coda Calibration

To accomplish full 2-D calibration capability in the coda methodology, we developed a new calibration technique for the 2-D envelope shape by applying a trans-dimensional hierarchical Bayesian tomography algorithm (Bodin et al., 2009; Bodin et al., 2012). We adopted the Bayesian tomography algorithm to map the posterior probability of modeling parameters used for the hybrid template modeling. The newly developed tomographic calibration technique allows us to estimate optimal shape parameters for the hybrid template for given source-receiver geometry and subsequent accurate explosion yields from small local events.

3.4.1 Trans-Dimensional Bayesian Framework

Conventional optimization scheme typically provides a single best-fit model while the fit of other models may only be slightly worse. For this reason, the optimization scheme does not well characterize the non-uniqueness and uncertainty of the model in most of cases. Also, the models often get stuck in local minima.

However, in Bayesian framework, the solution is given by large ensemble of models whose density is directly proportional to the posterior distribution of the model. This feature makes uncertainty analysis more simple and straight forward. Also, the sampling-based strategy of the Bayesian approach allows the model to jump out of the local minima and sample non-unique models (Khan *et al.*, 2011).

In most seismic tomography problems, Earth models are parameterized with a uniform local grid whose size is fixed a prior to the inversion. However, the information used for the tomography distributes unevenly in space due to the irregular source-receiver coverage. This leads to having an ill-posed condition in regions of poor path coverage. We usually deal with this condition by imposing regularization of the model parameters such as global smoothing, norm damping, or simply to coarsen the grid space. Although, the application of regularization often causes degrading resolution in the well-posed regions along with the ill-posed regions.

Most inverse problems in geophysics treat the number of unknown (e.g., number of grids, number of layers) as a constant. Trans-dimensional inversion is the name given to the case where this assumption is relaxed, and the number of unknown is treated as the unknown (Sambridge *et al.*, 2013). Bodin *et al.* (2009) first introduced the trans-dimensional parameterization to non-linear seismic tomography problem by implementing the Voronoi tessellation (Okabe *et al.*, 1992) and reversible jump Markov Chain Monte Carlo (rj-MCMC) algorithm (Green, 1995; Green and Mira, 2001; Sambridge *et al.*, 2006).

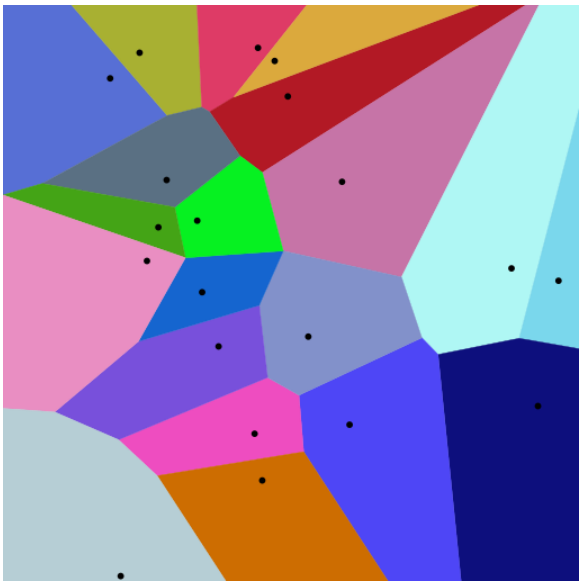

Figure 12. Example of Voronoi diagram, which forms a set of irregular cells that partition the plane. Any point inside a cell is closer to the node of that cell than any other node, so the shape of the parameterization is defined by the location of nodes (black dots) (wikipedia; https://en.wikipedia.org/wiki/Voronoi_diagram).

Figure 12 shows examples of the parameterization using the Voronoi cell. In mathematics, a Voronoi diagram is a partitioning of a plane into regions based on distance to points, called Voronoi nuclei, in a specific subset of the plane. These regions surrounded by the planes are called Voronoi cells. In the trans-dimensional tomography, the number and the location of the nuclei is unknown. The nuclei is mobile and can be newly created or destroyed so that the sizes and shapes of Voronoi cells also can be changed during the inversion.

The rj-MCMC algorithm allows inference on both model parameters and model dimensionality (Green, 1995). Rj-MCMC also called ‘birth-death MCMC algorithm and is an extension of the well-known Metropolis-Hastings algorithm (Matropolis *et al.*, 1953; Hastings, 1970). We implemented our tomography algorithm using the rj-MCMC software library by Rhys Hawkins at Australian National University (ANU).

3.4.2 Uncertainty in Data Noise and Hierarchical Bayes

Another difficulty in the seismic tomography problem is how to decide the level of data noise. In the geophysical inverse problem, how much noise is included in the data determines how much the inverted mode should fit the data, and finally determines the resolution of final model. It is very difficult to quantify this data noise in general. Therefore, in many cases, this value is determined arbitrarily by the users based on their prior knowledge and experience with the problem. As a result, the resolution of the resulting model is significantly affected by the user's judgment and intuition.

To address the limitations, Bodin *et al.* (2012) introduces the Hierarchical Bayesian inversion to the geophysical inverse problem. Similar to the Trans-dimensional method described above, this method also allows higher degree of freedom of the problem by treating the data noise as an

additional unknown term of the problem. Ultimately, it is the strength of this new approach that minimizes user involvement and ensures that all these decisions are determined by the input data itself.

3.4.3 Bayesian Mapping for the Scattering/Absorbing Parameters

The new hybrid modeling needs three model parameters, 1) characteristic time for the forward-scattering (t_M); 2) scattering coefficient for the coda exception ($g_0 = \frac{2\pi f}{vQ_s}$; $Q_S^{-1} = \frac{g_0 v}{2\pi f}$); 3) inelastic energy loss for the later coda decay rate (Q_i^{-1}). We have already implemented an algorithm that can extract optimal envelope modeling parameters for given waveform data by applying the Bayesian inversion technique to the hybrid envelope modeling. We completed developing the new trans-dimensional tomography algorithm and the coding to effectively map the extracted modeling parameters to 2-D space without distortion. Using the 2-D map of the envelope modeling parameters, we can find the optimal envelope modeling parameters for any given source-receiver path. This allows us to model a more accurate waveform template, which can be used to measure the accurate amplitude and eventually estimate the explosion yield.

Our new hybrid modeling technique is a more advanced method compared to the single back-scattering model widely applied in previous monitoring applications. However, it is still oversimplifying the real Earth. The analytic solutions included in the hybrid formula are derived for the homogeneous random half space. This ignores the stratigraphic characteristics of Earth's crust and the effect appears as distance dependence of the model parameters. 3-D mapping is required to take into account this layered property, but it is not realistic to apply 3-D calibration over a large area. In the previous 1-D coda calibrations, the distance dependency of the model parameters has been functionalized using hyperbolic curve fitting (Mayeda *et al.*, 1996; Mayeda *et al.*, 2003; Yoo *et al.*, 2011).

We follow the method proposed by Takahashi (2007) to correct the distance dependence of the model parameters. First, we find the linear dependence of the logarithm of modeling parameters against hypocentral distance,

$$\log_{10} t_M = A_{t_M} + B_{t_M} \log_{10} R$$
$$\log_{10} Q_S^{-1} = A_{Q_S^{-1}} + B_{Q_S^{-1}} \log_{10} R$$
$$\log_{10} Q_i^{-1} = A_{Q_i^{-1}} + B_{Q_i^{-1}} \log_{10} R$$

eq. 41

where t_M, Q_S^{-1} and Q_i^{-1} are the modeling parameters for the hybrid envelope modeling, R is the hypocentral distance, A and B are regression coefficients. Then, we define the logarithmic deviation of each model parameter from the regression line as,

$$\Delta\log_{10} t_M = \log_{10} t_M - A_{t_M} - B_{t_M} \log_{10} R$$
$$\Delta\log_{10} Q_S^{-1} = \log_{10} Q_S^{-1} - A_{Q_S^{-1}} - B_{Q_S^{-1}} \log_{10} R$$
$$\Delta\log_{10} Q_i^{-1} = \log_{10} Q_i^{-1} - A_{Q_i^{-1}} - B_{Q_i^{-1}} \log_{10} R$$

eq. 42

where $\Delta\log_{10}t_M$, $\Delta\log_{10}Q_S^{-1}$, and $\Delta\log_{10}Q_i^{-1}$ are the values for the Bayesian tomographic mapping. Our current interpretation for these values are the strength of scattering/absorbing due to the heterogeneities along the source-receiver path (e.g., Pezzo et al., 2016). Thus, the values are given by,

$$\Delta\log_{10}t_{M_n} = \frac{1}{R}\sum_m \Delta\log_{10}t_M{}^m \cdot dr^{m,n}$$

$$\Delta\log_{10}Q_S^{-1}{}_n = \frac{1}{R}\sum_m \Delta\log_{10}Q_S^{-1}{}^m \cdot dr^{m,n}$$

$$\Delta\log_{10}Q_i^{-1}{}_n = \frac{1}{R}\sum_m \Delta\log_{10}Q_i^{-1}{}^m \cdot dr^{m,n}$$

eq. 43

where $\Delta\log_{10}t_{M_n}$, $\Delta\log_{10}Q_S^{-1}{}_n$, and $\Delta\log_{10}Q_i^{-1}{}_n$ are the values of ray n, and $\Delta\log_{10}t_M{}^m$, $\Delta\log_{10}Q_S^{-1}{}^m$, and $\Delta\log_{10}Q_i^{-1}{}^m$ are the model parameters assigned to cell m, and $dr^{m,n}$ is the length of ray n across cell m.

3.4.4 Comparison between Conventional and Bayesian Tomography Techniques

We conducted synthetic tests that compared the trans-dimensional Bayesian approach with a conventional optimization using the Least Square (LSQR) method. We did not develop a separate LSQR tomography code for the comparison study. Therefore, we used the Fast Marching Surface Tomography (FMST) Package to simulate the conventional optimization results and then modified our Bayesian tomography code to solve the velocity structure for given travel time and ray travel path.

The synthetic data used in the comparison was calculated for a 5º× 5º checkerboard model with a variation of ±0.25 km/s in a homogeneous model with an average velocity of 5 km/s (Figure 13). We added 1 second standard deviation of Gaussian random noise to the synthetics. We note that only 1000 ray paths are used for each tomography inversion considering low seismicity in the study area.

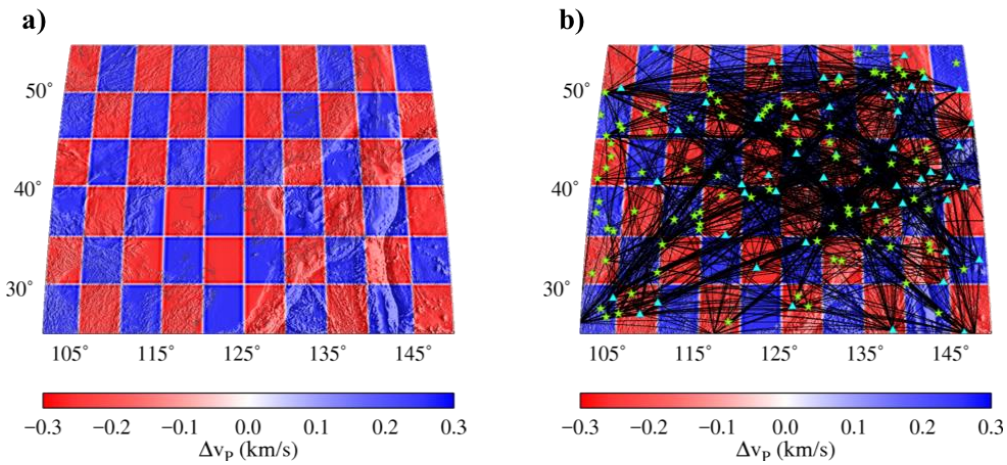

Figure 13. a) Synthetic model b) ray coverage for a checkerboard test. Stars, triangles and black lines represent sources, receivers, and rays between the source and receiver, respectively.

Figure 14 shows the results of the conventional optimization for three different model parameterizations, 1º×1º, 2º×2º, and 5º×5º, respectively. The optimal regularization for smoothing and norm damping were determined by the L-curve test for each case.

First, we need about 1600 model parameters for the case of 1º×1º grid space, which is more than the 1000 ray paths of data given. Despite our efforts to choose optimal level of regularization, the highly ill-posed condition lead to serious overfitting of the data. Estimated data noise from the final model is 0.7s, which is smaller than 1 s used for the synthesis of the data.

In the case of a 5º×5º grid space, on the other hand, we only need about 70 model parameters, which is much less than the number of data given. However, it is too coarse of a grid to resolve the given checkerboard model and results in underfitting. Estimated data noise from the final model is 3.8s, which is much larger than 1 s used for synthesizing the data

In the case of 2º×2º grid space we need 400 model parameters, and we obtained the most satisfactory recovery result. The data noise estimated from this model is approximately 1s, which is almost identical to the value used in the actual synthetics. Even in this case, there are still distorted results in regions with poor ray coverage. All the cases failed to recover the sharp discontinuity of the checkerboard synthetic model.

The trans-dimensional Bayesian tomography provided a much more accurate checkerboard recovery result compared to the conventional method (Figure 15). Estimated average of number of model parameters is about 220, and estimated data noise by the hierarchical algorithm is about 1.07 s, which is very close to 1 s used in synthetic data.

The Bayesian inversion method provided reasonable recovery even in regions with poor ray coverage. In addition, the discontinuity of the checkerboard synthetic model is very well recovered. Note that model uncertainty can be directly calculated from the posterior distribution of the model parameters, which is very important information for interpreting the model and applying the model for other applications.

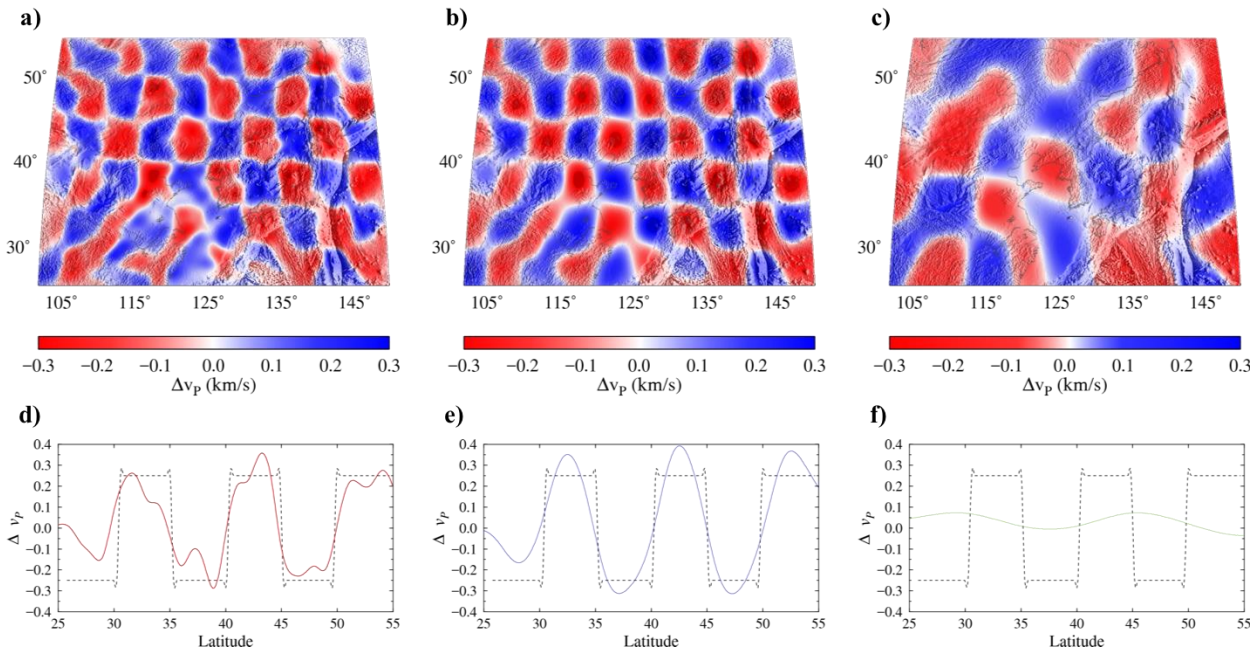

Figure 14. Results of the checkerboard recovery test using a) 1º×1º, b) 2º×2º, and c) 5º×5º grid spaces, respectively. Dotted and solid lines in d), e), and f) show the profile at 127.5º of synthetic and recovered models from each case.

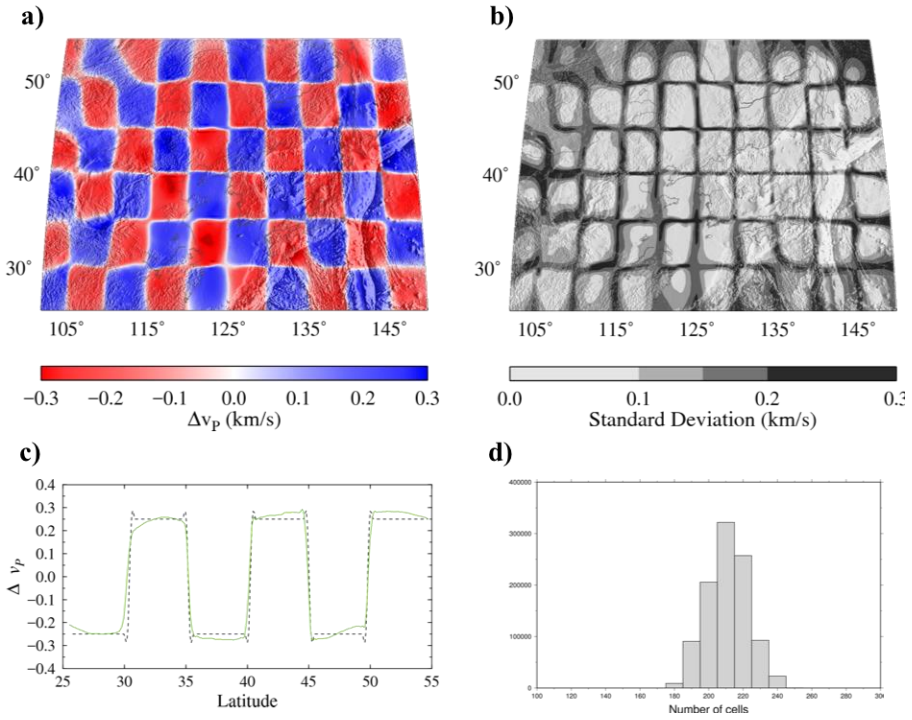

Figure 15. a) Recovered model and b) estimated uncertainty of the checkerboard test using the trans-dimensional Bayesian tomography. Dotted and solid lines in c) show the profile at 127.5º of synthetic and recovered models. d) A histogram of number of cells in the Voronoi tessellation.

4.0 RESULTS AND DISCUSSION

4.1 Application to North East Asia and North America

As a preliminary study, we have applied the developed Bayesian tomography code to data obtained from the Korean Peninsula (AFRL contract FA9453-16-C-0022) and North America (AFRL contract FA9453-16-C-0023). Due to the low seismicity of the Korean Peninsula, the amount of data that has been collected and processed so far is not enough to obtain the high resolution of calibration for the envelope shape parameters (Figure 16). We found strong scattering and high intrinsic attenuation in the Japan area and weaker scattering and lower intrinsic attenuation in the Korean Peninsula and Northeast China. We also found some good spatial correlation of the intrinsic attenuation to the direct *Lg* Q result from the direct wave tomography inversion. However, the data included in the current test do not have many paths crossing the East Sea (Sea of Japan), thus the inversion of this region is very poor. If we add more data for the remaining research period of FA9453-16-C-0022, we expect the final results to be improved significantly by end of the project.

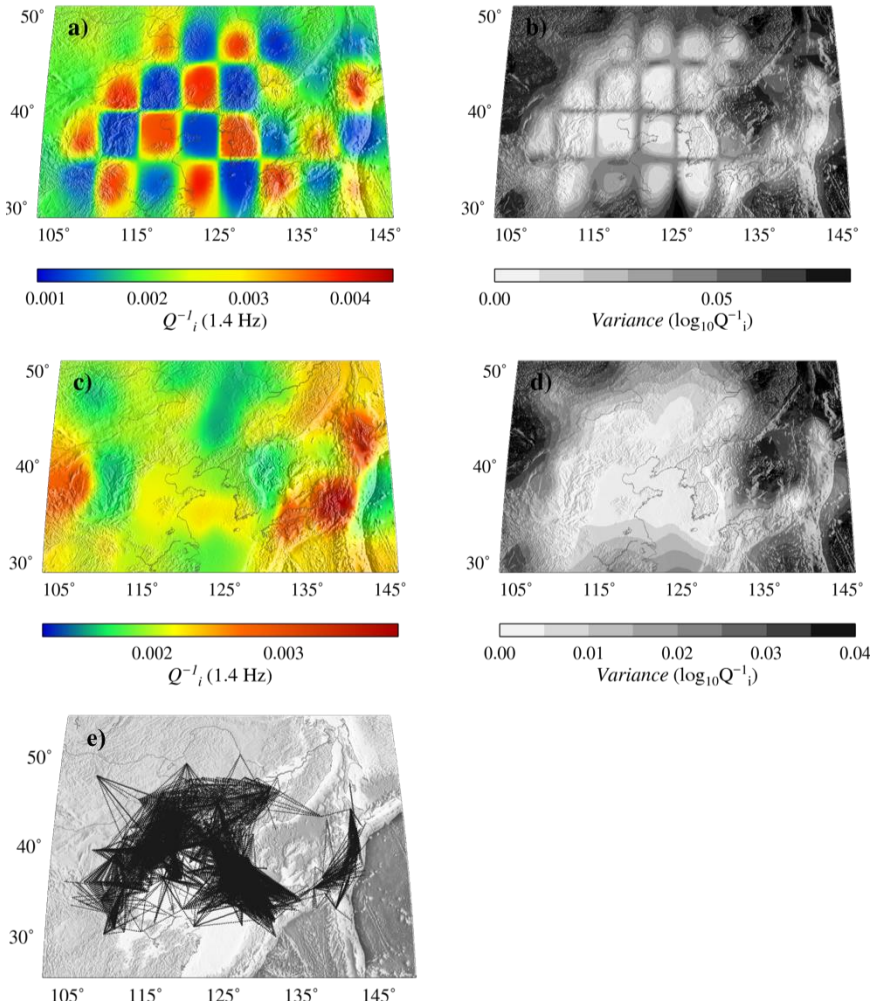

Figure 16. a) and b) show a checkerboard recovery and uncertainty using source-receiver paths shown in e), respectively. c) and d) show tomography results and corresponding uncertainty estimates of the inelastic energy loss (Q_i^{-1}) at 1.4 Hz.

We also started to apply the trans-dimensional Bayesian tomography to the North America region. We were able to collect and process sufficient data for the North America region. Figure 17 shows a distribution of the hybrid modeling parameters for the North America region. We can identify the vast difference between the West and the East, and the predicted envelop model expresses the actual data well (Figure 18).

At the end of the program, the developed Bayesian tomography code will be applied to the two AFRL funded projects and will contribute significantly to predict more accurate seismic amplitudes and explosion yield estimates with rigorous uncertainty estimates.

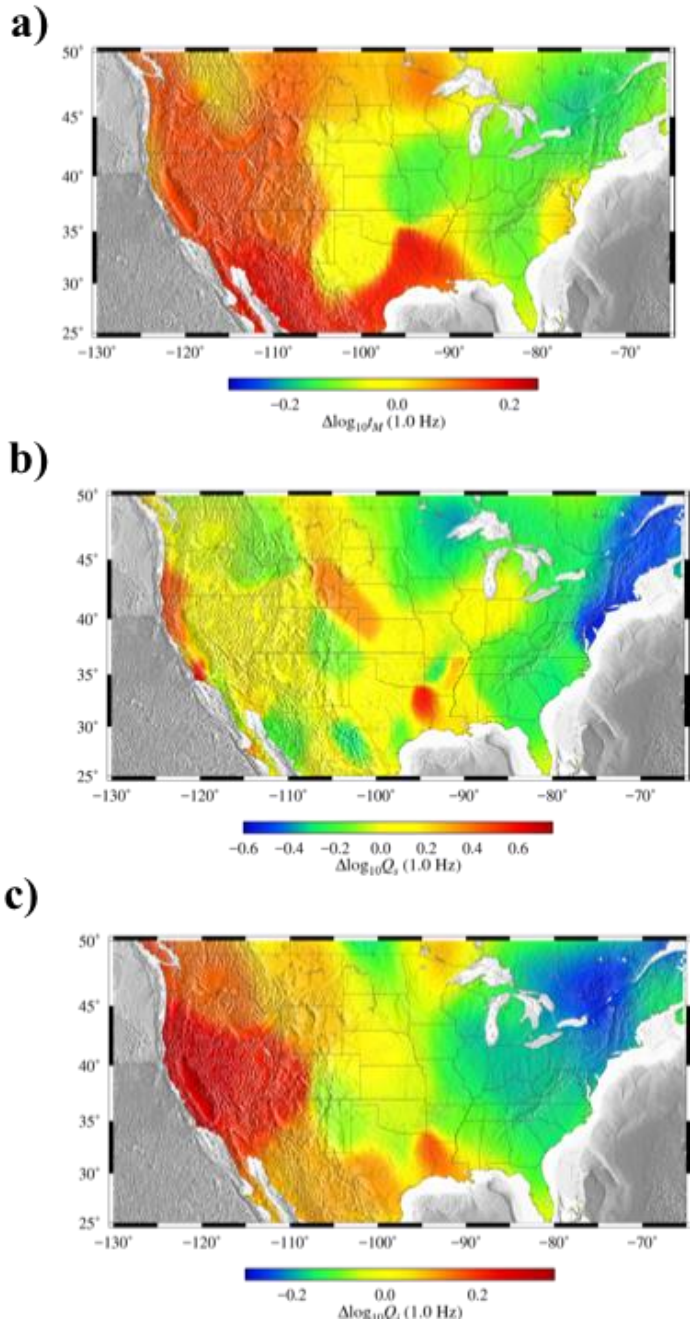

Figure 17. a) characteristic time, b) scattering coefficient, c) inelastic energy loss at 1 Hz.

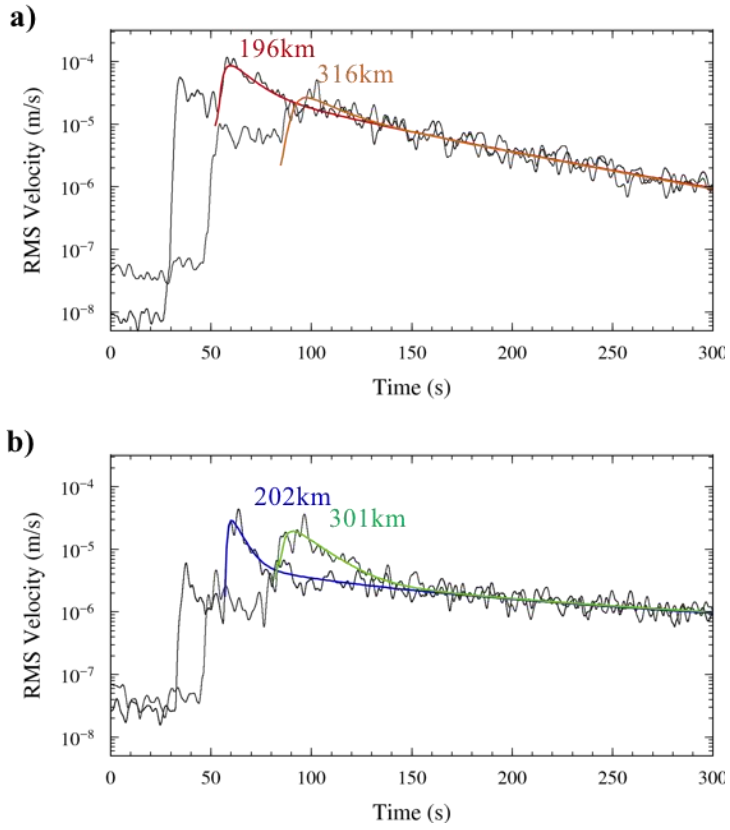

Figure 18. 1-Hz narrowband envelopes of a) a M 4.9 earthquake near California and Nevada border on 1997/11/02 08:51:54 recorded at CMB (red) and SCZ (orange), and b) a M 4.7 earthquake near Ottawa, Canada on 2013/05/17 13:43:22 recorded at WCNY (blue) and HBVT (green). Colored lines show the predicted synthetics using model parameters in Figure 6.

4.2 Full-Waveform Envelope Templates for Discrimination and Yield Estimation

A new hybrid envelope modeling method with the Bayesian sampling method developed under this contract became a major step in AFRL funded research projects. We have developed a new discrimination and yield estimation method known as full-waveform envelope template matching to improve predicted envelope fits over the entire waveform and account for direct-wave and early coda complexity. We accomplished this by including a multiple forward-scattering approximation in the envelope modeling of the early coda. The new hybrid envelope templates are designed to fit local and regional full waveforms and produce low-variance amplitude estimates, which improve yield estimation and discrimination between earthquakes and explosions.

To demonstrate the new technique, we applied our full-waveform envelope template-matching method to the six known North Korean (DPRK) underground nuclear tests. We successfully discriminated the event types and estimated the yield for all six nuclear tests. We also applied the same technique to the 2015 Tianjin explosions in China, and another suspected low-yield explosion at the DPRK test site on 12 May 2010. Our results show that the new full-waveform envelope template-matching method significantly improves upon longstanding single-scattering coda prediction techniques. More importantly, the new method which is possible using the

hybrid envelope modeling method with the Bayesian sampling method allows monitoring seismologists to extend coda-based techniques to lower magnitude thresholds (m_b < 4) and low-yield local explosions.

4.2.1 Application to the North Korean Nuclear Tests

Figure 19 shows waveform envelopes and matched hybrid synthetics for the 3 September 2017 DPRK nuclear test recorded at two Korea Meteorological Administration (KMA) seismic stations: Mudanjiang (MDJ) and Inchon (INCN). The new hybrid model fits the crustal *Pg* and its coda very well for broad range of frequency bands. We measured the template amplitudes from the template matching and corrected for path attenuation, site amplification and the coda transfer function obtained from the 2D calibration (see the third status report for details) and estimated the source spectra.

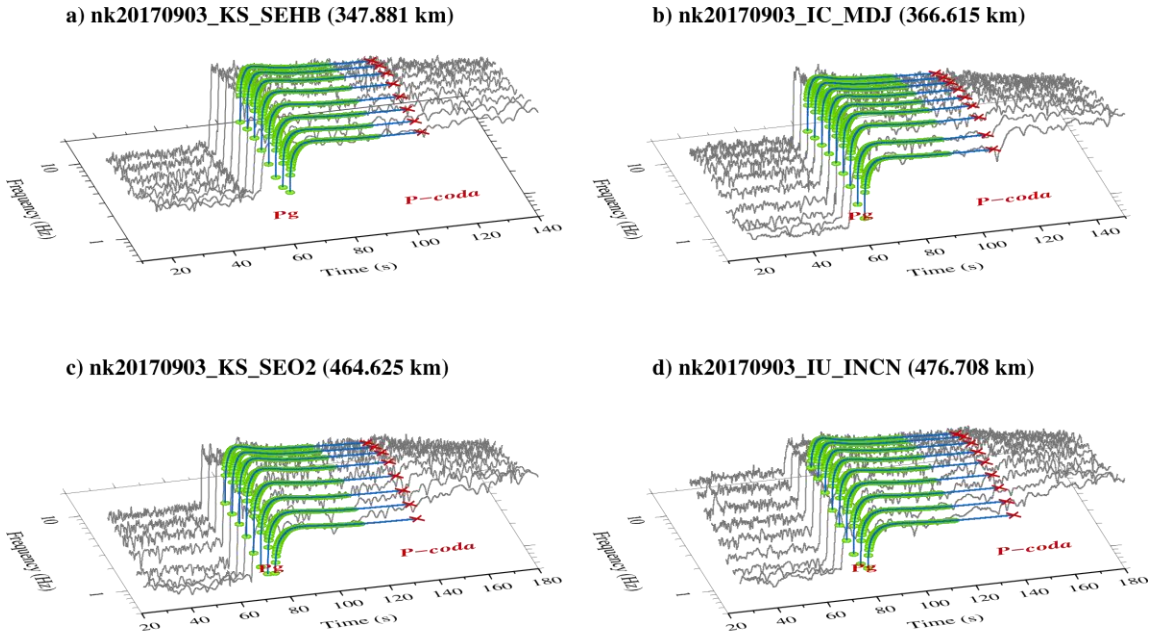

Figure 19. An example of observed full-waveform envelopes (thin gray lines) that match the new synthetic templates (green circles) for 3 September 2017 DPRK nuclear test event. Blue lines and red crosses represent the noise-corrected synthetics and template amplitudes, respectively.

Figure 20 show the estimated source spectra of crustal earthquakes, DPRK nuclear tests, and another suspected low-yield explosion at the DPRK test site on 12 May 2010. The crustal earthquakes show very comparable source spectra from both P- and S-template matching and we were able to fit the spectra with Brune source model (Brune, 1970). For the nuclear tests, on the other hand, source spectra from P-template matching are scientifically differ from source spectra from S-template matching. The explosion source model (MM71; Mueller and Murphy, 1971) provides better fit to the P-source spectra than the Brune model. Assuming a granite near the source region and depth of burial is scaled to yield (an empirical model described in Stevens and Day, 1985), we estimated yields for all six nuclear tests, 0.67 kt at 106.8 m for 2006 test, 3.25 kt

at 180.7 m for 2009 test, 9.36 kt at 257.1 m for 2013 test, 6.64 kt at 229.3 m for January 2016 test, 11.64 kt at 276.m for September 2016 test and 154.89 kt at 655.2 m for September 2017 test. We note that depth is a dependent variable, not an estimate in our result. The yield estimates will be higher for deeper depth.

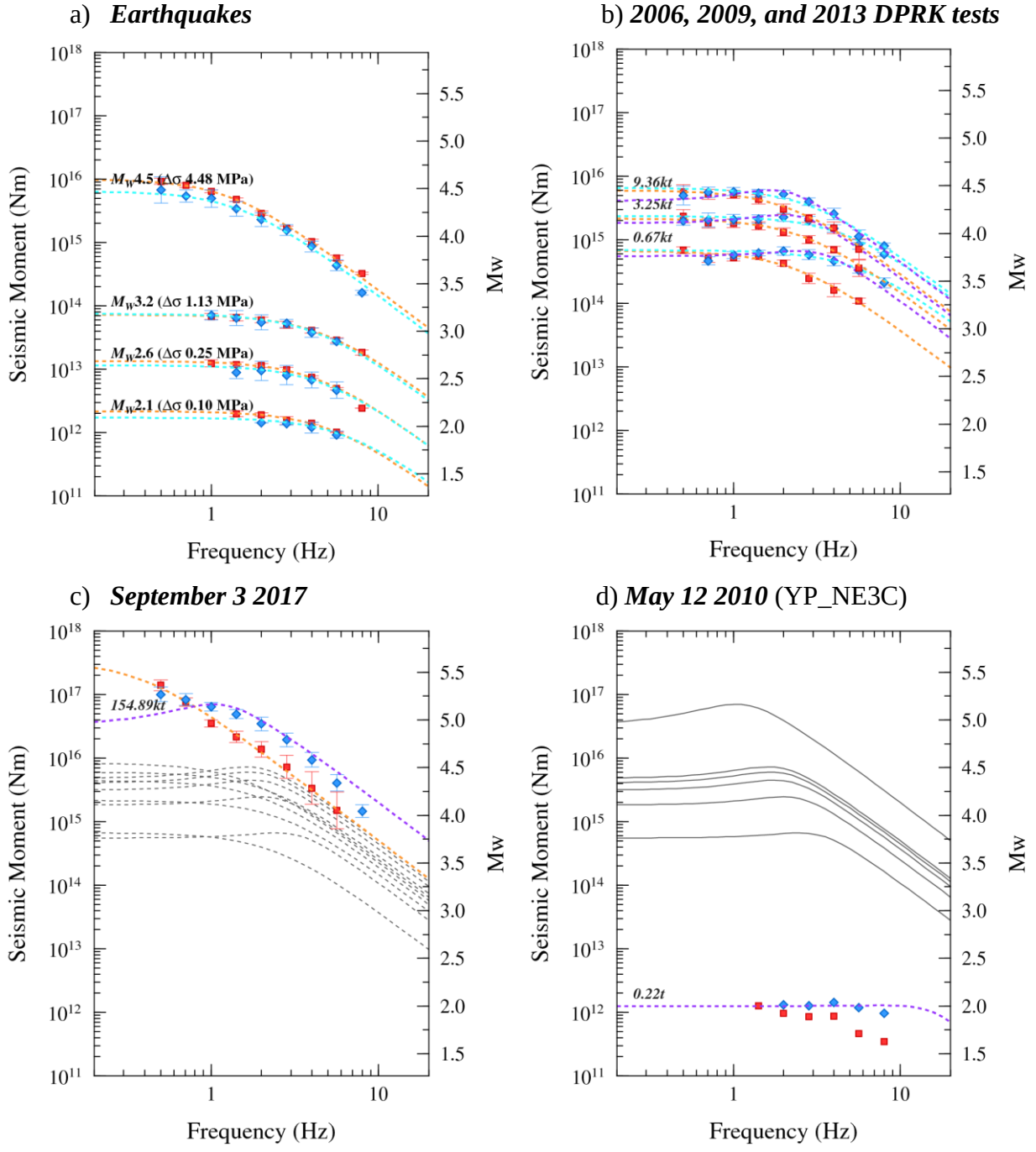

Figure 20. Source spectrum comparison between a) earthquakes, b) 2006, 2009, 2013 DPRK tests, c) 3 September 2017 event, and d) 12 May 2010 event. Blue diamonds and red squares represent estimated source spectra using P- and S- template matching, respectively. We note that the result of the 12 May 2010 event is a single station estimate at NE3C station (~164 km).

4.2.2 Yield estimation of the suspected low yield event on May 12 2010

We analyzed the suspected low-yield nuclear event on 12 May 2010 recorded on the Dongbei Broadband Network (DBN; Chun et al., 2011). The data was provided by Professor Paul Richards (Columbia University) and also included the 2006 and 2009 North Korea Nuclear Tests.

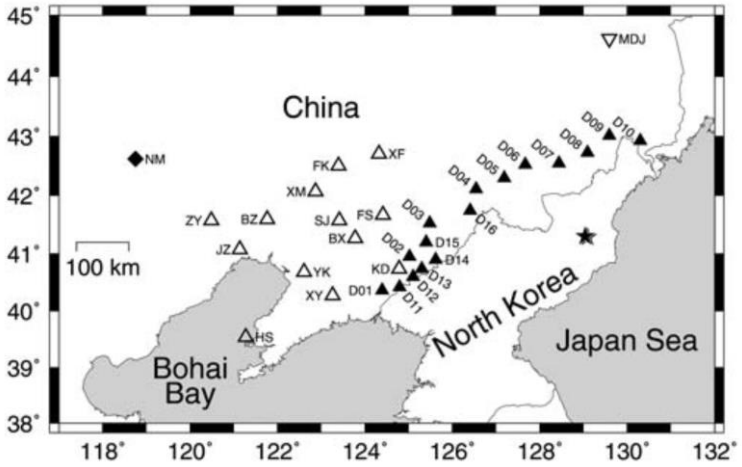

Figure 21. Map showing the North Korean nuclear test site (star) and the seismic stations in the Dongbei Broadband Network (solid triangle) (Chun et al., 2011, copyright by the Seismological Society of America).

The locations of the stations in the network are shown in Figure 21 represented by black triangles. The nearest station to the North Korean nuclear test center is about 1.34 degrees. For now, this is the closest distance we can obtain.

Compared to 2006 and 2009 events, both P and S amplitudes of the 2010 event are very small and most of coda signals are below the noise level (Figure 22). Only direct waves and some portion of early coda signals appear to be available for further analysis.

We applied the measured amplitudes to the preliminarily amplitude attenuation models and reconstructed its source spectrum. Then, we applied the MM71 explosion source model to estimate the yield and depth of burial (Mueller and Murphy, 1971). Due to the very small size compared to other nuclear tests, the corner frequency will be beyond the limit of the calibration band. This lack of high frequency source spectrum made it difficult to predict the yield and depth simultaneously using the explosion model. Therefore, we estimated the yields according to two assumptions listed below to calculate the two depths used in the MCMC inversion (Figure 23).

First, assuming the explosion depth follows the 122m/kt^3 scaling (e.g., Stevens and Day, 1985), the explosion yield is equivalent to about 200kg of TNT at 7m below ground. However, if we assume the depth to 200 m deep, the yield estimate is as high as 700 kg TNT. Even assuming we have similar depths to other DPRK nuclear tests, yield estimates do not appear to be higher than 1 ton. Our finding is in good agreement with the conclusions reached by Ford and Walter (2014) through analysis of the IMS networks around the North Korean nuclear test site.

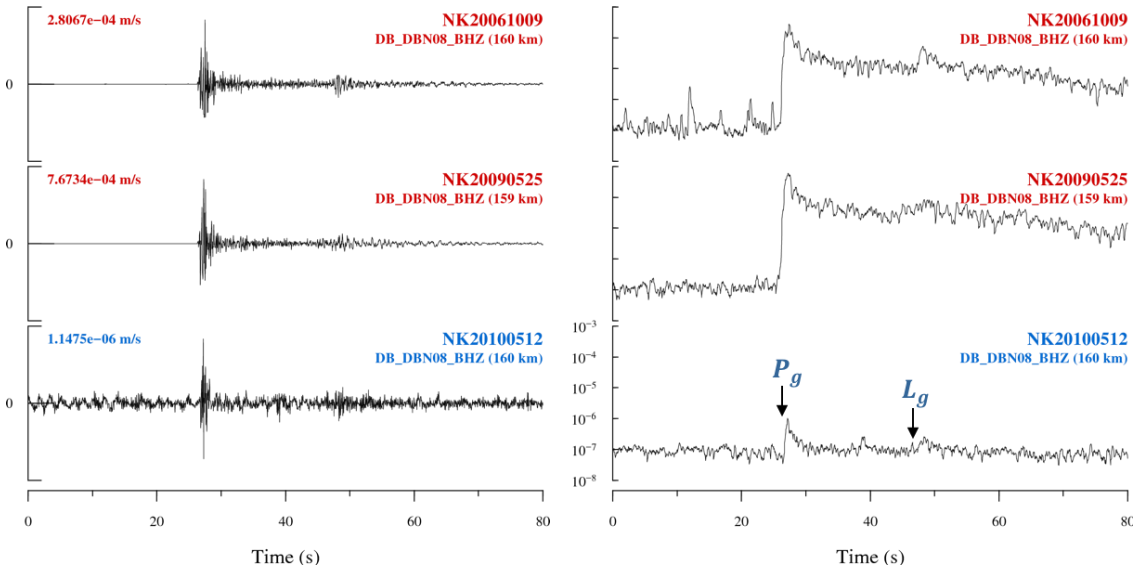

Figure 22. Vertical component waveform (left) and the narrowband envelope (right) of the observed the 2006, 2009, and 2010 events recorded at DBN08.

Our hybrid envelope model not only has superior data representation for such a short coda signal, but also can be applied to data with a very low signal-to-noise ratio by parameterizing the noise in the model. We were able to make template amplitude measurements at four stations in the DBN for the 2010 event.

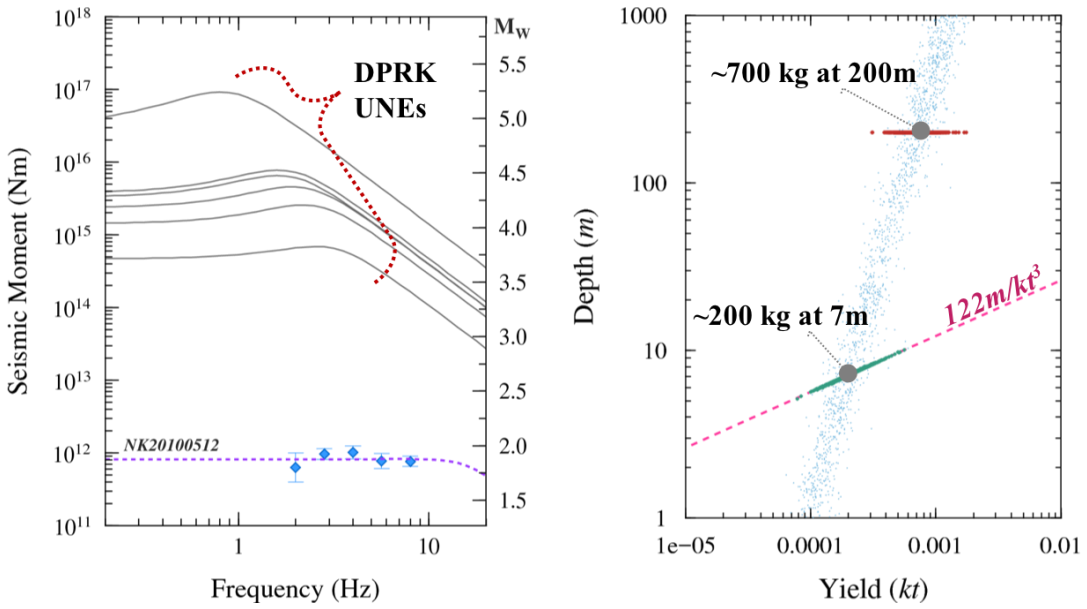

Figure 23. (left) The recovered source spectrum of the 2010 May event (blue diamond) along with the best fit of MM71 source models for the six North Korean nuclear tests (solid line). (right) The posterior distribution of yield and depth estimates from the Markov-Chain Monte Carlo inversion (blue dot) using the two assumed depths of 7m and 200m. Green and red symbols represent the posterior distribution of the estimates assuming the 122m/kt^3 scaling and 200m fixed depth, respectively.

4.3 3-D Full-waveform Simulations for the North Korean Nuclear Tests

In other work we are using 3-D spectral element methods (SEM) to simulate the effects of varied depths-of-burial for explosions detonated in mountainous terrain. The goal behind the modeling efforts is to look for the imprint of topography on far-field seismic observations, which could eventually lead to improved estimates of seismic explosion yield. The five nuclear explosions detonated in North Korea (NK) provided an excellent test bed for this exercise.

In Figure 24a we show a map view of the surface topography over the test site. The red square indicates the surface area where we extracted a Shuttle Radar Topography Mission (SRTM) 90-m digital elevation map that we used to generate a 3-D spectral-element mesh with 200-m sampling. We note that SEM meshes do not require the fine-scale grid sampling needed by finite-difference codes; e.g., a 200-m meshing interval in SPECFEM3D (open source SEM code at https://geodynamics.org/cig/software/specfem3d/) can simulate the same wavefields as a 50-m grid interval in finite-difference modeling. The 3-D mesh we input to SPECFEM3D covered a 40-km x 40-km x 20-km region (inset view shown in the upper left corner of Figure 24b). Figure 24b also shows a close-up oblique view of the mesh topography with Mt. Mantap and the North Portal indicated with arrows.

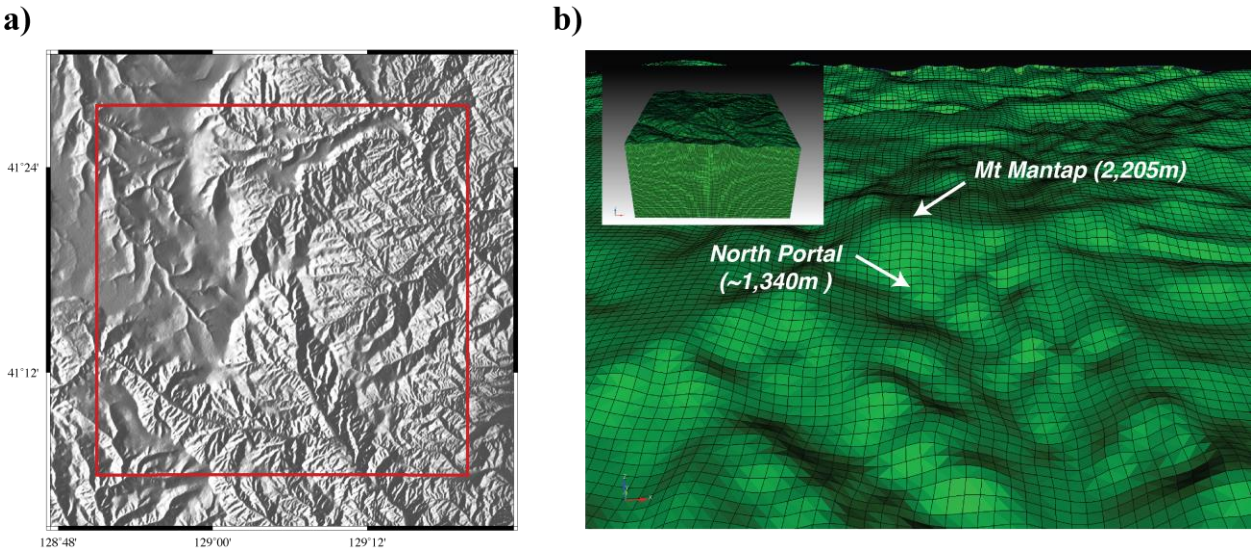

Figure 24. a) Map view of topography near the North Korean Test Site from SRTM 90-m digital elevation data (http://srtm.csi.cgiar.org) and b) an associated 3-D spectral-element mesh (40km x 40km x 20km). We used a 200-m sampling interval in the spectral-element mesh design, which is equivalent to a ~50-m grid sample size in a finite-difference modeling approach.

For this demonstration we chose a simple velocity model to isolate the effect of mountainous topography on the simulated waveforms. We generated a homogeneous velocity model with values of 5190 m/s, 3000 m/s and 2500 kg/m^3 for the *P* velocity, *S* velocity and density, respectively. These fast wave speeds correspond to the presumed granitic geology around the test site (e.g., Ford *et al.*, 2009; Rodgers *et al.*, 2010).

Figures 25 and 26 illustrate how regional observations in mountainous terrain could be exploited for depth estimation, with waveform data from the 2009 DPRK nuclear test. Figure 25a shows a comparison of the SPECFEM3D flat- and rough-topography synthetics from the model in Figure

24b at regular azimuthal intervals and a 10-km observation distance. The flat-topography waveforms are plotted in black, and the rough-topography results in green. There are clear differences in the rough-topography waveforms as a function of azimuth, particularly in the *P* and *pP* arrival packets (denoted and highlighted inside a gray-shaded annulus).

Figure 25b shows the vertical-component seismograms from the 2009 NK explosion observed at stations MDJ and KSA, which recorded the event at azimuths and distances of 7° (371 km) and 191° (307 km), respectively. Because the depth-phase time delay (*pP*-*P*) is nearly invariant to range, it is meaningful to compare synthetics at 10 km to observations at 300+ km. There is a remarkable match between the rough-topography synthetics and the station observations at their corresponding azimuths. Compared to the initial *P* phase, the depth phase *pP* at station MDJ is enhanced while *pP* at station KSA is significantly weaker. As expected, this depth-phase enhancement does not occur in the flat-topography synthetics, but is present in the synthetics that simulate the topography at the NK test site.

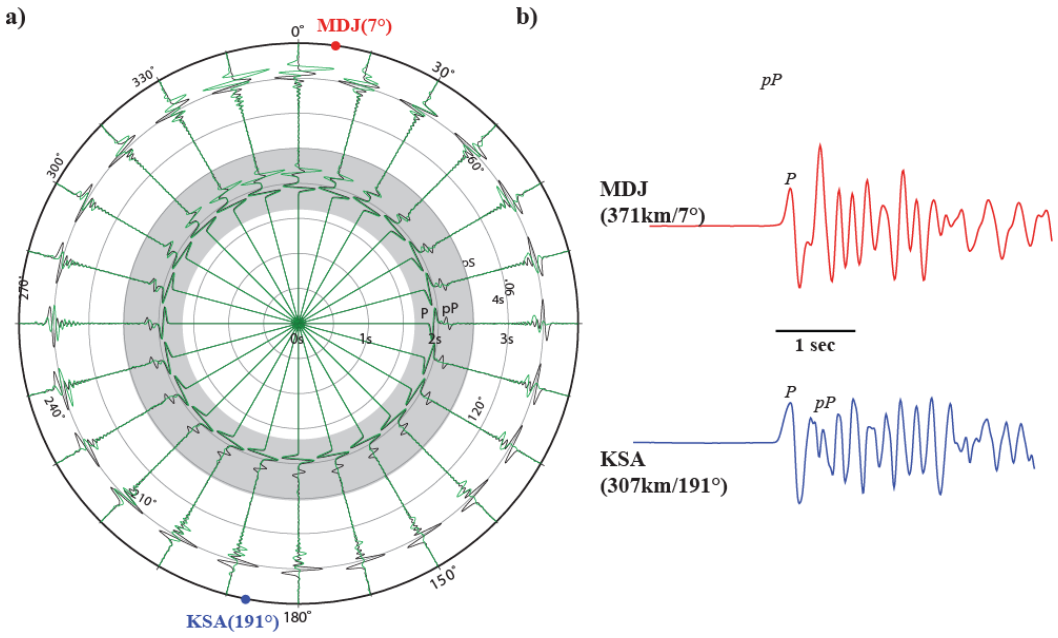

Figure 25. a) SPECFEM3D waveform synthetics observed at 10 km from a source with a 45° takeoff angle; green waveforms produced by the rough-topography simulation, black by flat-topography situation. b) The observed vertical-component velocity seismograms at the Mudanjiang (MDJ) and Ganseong (KSA) stations for the 2009 NK nuclear explosion. The behavior of the *P* and *pP* arrivals in the rough-topography synthetics matches the observed waveforms well at the MDJ and KSA azimuths. Note that the synthetic waveforms are down-going and thus have ‘down’ first motions.

Figure 26 provides a theoretical explanation for why the 3-D rough-topography synthetics match the observations in this case. Depth phases at observations on the north side of the mountain exhibit larger amplitudes and phase delays with respect to the direct P arrivals, compared to the weaker (or nonexistent) depth phases to the south. This might imply the depth phases to the north experience a focusing effect from curved/asymmetric free surface of Mt Mantap (i.e., analogous to the foci of a hyperbola).

In future efforts we will analyze synthetic waveforms to identify waveform phenomena that are diagnostic of source depth. Rough free-surface topography will make the waveforms more complex, but could potentially produce useful constraints on source depth – provided the effects of the topography can be observed and interpreted in data.

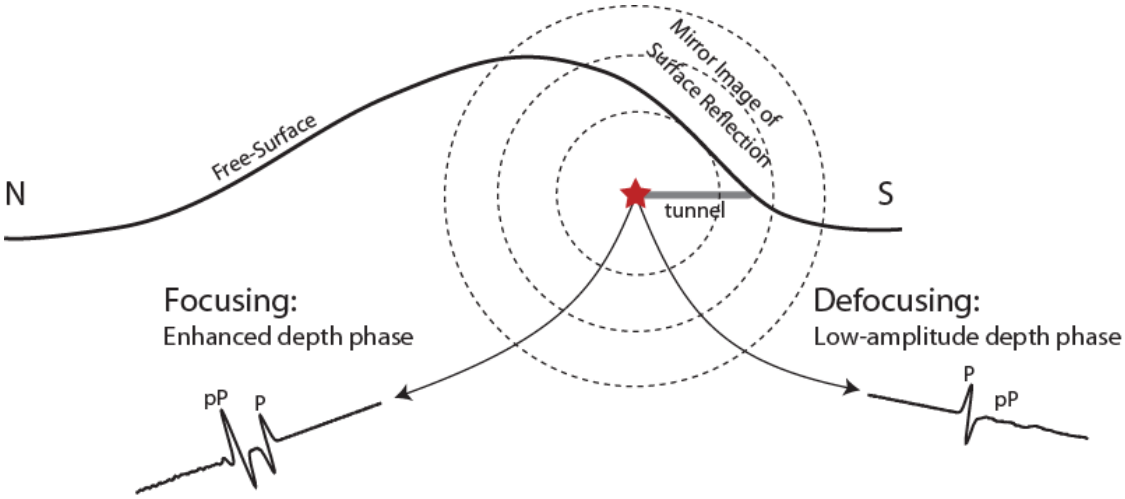

Figure 26. Two-dimensional illustration of focusing/defocusing observed in depth phases generated in mountainous terrain. The elongated lens-like (or dome-like) mountain surface generates a complicated reflection of the depth phase that can be tracked azimuthally. For the example shown in Figure 3, station MDJ is to the north (enhanced *pP*) and station KSA is to the south (low-amplitude *pP*).

5.0 CONCLUSIONS

We developed a new Bayesian calibration technique for the 2-D envelope shape correction to accomplish full 2-D calibration capability in the coda methodology and to improve yield estimation for small underground explosions.

The joint R&D efforts under this U.S. Department of State's V-FUND and other AFRL contracts allowed us to implement two significant and innovative upgrades to the conventional coda methodology, 1) a new hybrid waveform envelope modeling technique and 2) a 2-D calibration approach that includes both the envelope shape and amplitude attenuation.

The full-waveform measurement approach based on the new hybrid modeling technique allows accurate amplitude measurements and subsequent yield estimates from small local explosions. The full 2-D calibration approach based on the Trans-Dimensional Bayesian Tomography algorithm extends the traditional coda calibration to have full 2-D capability to improve complex, broad area calibrations (e.g., Iran)

Our combined R&D development efforts are producing significantly improved fits to shorter-length signals from smaller events, as well as more accurate yield estimates. The new processing technique is also shifting conventional coda-based analysis from a strictly empirical basis to a physical one. These improvements have been long-term goals of significant interest to U.S. monitoring agencies.

6.0 REFERENCES

Bodin, T. and Sambridge, M. (2009), Seismic tomography with the reversible jump algorithm. Geophysical Journal International, 178: 1411-1436. doi:10.1111/j.1365-246X.2009.04226.x

Bodin, T., Sambridge, M., Rawlinson, N. and Arroucau, P. (2012), Transdimensional tomography with unknown data noise. Geophysical Journal International, 189: 1536-1556. doi:10.1111/j.1365-246X.2012.05414.x

Bonner, J. L., D. R. Russell, and R. E. Reinke (2013). Modeling surface waves from aboveground and underground explosions in alluvium and limestone, *Bull. Seismol. Soc. Am.* 103, 2953–2970, doi: 10.1785/0120130069.

Brune, J. (1970), Tectonic stress and the spectra of seismic shear waves from earthquakes, *J. Geophys. Res.* 75, 4997-5009. (Correction, *J. Geophys. Res.* 76, 5002, 1971.)

Chung, T. W., K. Yoshimoto, and S. Yun (2010), The separation intrinsic and scattering seismic attenuation in South Korea, *Bull. Seismol. Soc. Am.* 100, 3183–3193.

Green, P., 1995. Reversible jump MCMC computation and Bayesian model selection, *Biometrika*, **82,** 711–732.

Green, P. & Mira, A., 2001. Delayed Rejection in Reversible Jump Metropolis-Hastings, *Biometrika*, **88**(4), 1035–1053.

Fehler, M., H. Sato, and L.-J. Huang (2000), Envelope broadening of outgoing waves in 2-D random media: A comparison between the Markov approximation and numerical simulations, *Bull. Seismol. Soc. Am.*, 90, 914– 928.

Ford S. R., W. R. Walter; International Monitoring System Correlation Detection at the North Korean Nuclear Test Site at Punggye-ri with Insights from the Source Physics Experiment. *Seismological Research Letters* ; 86 (4): 1160–1170. doi: https://doi.org/10.1785/0220150029

Hastings, W.K. (1970), Monte Carlo Sampling Methods Using Markov Chains and Their Applications, *Biometrika*, 57 (1), 97–109.

Hoshiba, M. (1994), Simulation of coda wave envelope in depth dependent scattering and absorption structure, *Geophys. Res. Lett.*, 21, 2853–2856.

Kanu, C., and R. Snieder, (2015), Numerical computation of the sensitivity kernel for monitoring weak changes with multiply scattered acoustic waves, Geophysical Journal International, 203,1923-1936.

Khan, A., A. Zunino, and F. Deschamps (2011), The thermo-chemical and physical structure beneath the North American continent from Bayesian inversion of surface-wave phase velocities, *J. Geophys. Res.*, 116, B09304, doi:10.1029/2011JB008380.

Kim, S., J. Dettmer, J. Rhie, and H. Tkalčić, Hrvoje (2016), Highly efficient Bayesian joint inversion for receiver based data and its application to lithospheric structure beneath the southern Korean Peninsula, *Geophysical Journal International*, 206(1), 328-344.

Mayeda, K. and W.R. Walter (1996), Moment, energy, stress drop, and source spectra of western U.S. earthquakes, *J. Geophys. Res.*, **101**, 11195-11208.

Mayeda, K., Hofstetter A., O'Boyle J. L., Walter, W. R., (2003), Stable and transportable regional magnitudes based on coda-derived moment-rate spectra. *Bull. Seismol. Soc. Am.*, **93**, 224-239.

Mayeda, K., Malagnini, L., Phillips, W. S., Walter, W. R., Dreger, D. (2005), 2-D or not 2-D, that is the question: A northern California test, *Geophys. Res. Lett.*, VOL. 32, L12301, doi:10.1029/2005GL022882.

Mayor, J., L. Margerin., and M. Calvet, (2014), Sensitivity of coda waves to spatial variations of absorption and scattering: radiative transfer theory and 2-D examples, Geophysical Journal International, 197, 1117–1137.

Metropolis, N., Rosenbluth, A., Rosenbluth, M., Teller, A. & Teller, E., (1953), Equation of state calculations by fast computing machines, *J. Chem. Phys.*, 21(6), 1087–1092.

Morse, P. M. and H. Feshbach (1953), Methods in Theoretical Physics, *McGraw- Hill*, Boston.

Mueller, C. S., and J. R. Murphy (1971). Seismic characteristics of under- ground nuclear detonations, Part I: seismic spectrum scaling, *Bull. Seism. Soc. Am.* **61,** 1675–1692.

Okabe, A., Boots, B. & Sugihara, K., 1992. *Spatial Tessellations: Concepts and Applications of Voronoi Diagrams*, John Wiley & Sons, Inc., New York, NY, USA.

Paasschens JCJ (1997) Solution of the time-dependent Boltzmann equation. *Phys Rev E* 56(1):1135–1141, DOI 10.1103/PhysRevE.56.1135.

Pasyanos, M.E., Walter, W.R., and Mayeda, K. (2012), Exploiting regional amplitude envelopes: A case study for earthquakes and explosions in the Korean Peninsula, *Bull. Seism. Soc. Am.*, 101, 2388-2398, 10.1785/0120120012.

Saito, T., H. Sato, and M, Ohtake (2002), Envelope broadening of spherically outgoing waves in three-dimensional random media having power law spectra, *J. Geophys. Res*, **107**, B5, do: 10.1029/2001JB000264.

Saito, T., H. Sato, M. Fehler, and M. Ohtake (2003), Simulating the envel- ope of scalar waves in 2D random media having power-law spectra of velocity fluctuation, *Bull. Seismol. Soc. Am.*, 93, 240–252.

Sambridge M., T. Bodin, K. Gallagher, H. Tkalcic (2013), Transdimensional inference in the geosciences, Philos Trans A Math Phys Eng Sci., 371(1984):20110547. doi: 10.1098/rsta.2011.0547

Sambridge, M., Gallagher, K., Jackson, A. & Rickwood, P., 2006. Trans- dimensional inverse problems, model comparison and the evidence, *Geo- phys. J. Int.*, **167**(2), 528–542.

Sanborn, C.J. (2015). Radiative3D: http://rainbow.phys.uconn.edu/geowiki/Radiative3D.

Sato, H., M. C. Fehler, and T. Maeda (2012), Seismic Wave Propagation and Scattering in the Heterogeneous Earth: Second Edition, Springer.

Sato, H., 2016. Envelope broadening and scattering attenuation of a scalar wavelet in random media having power-law spectra, *Geophys. J. Int.*, 204(1), 386–398.

Sato, H., M. Fehler, and Saito T (2004) Hybrid synthesis of scalar wave envelopes in two-dimensional random media having rich short-wavelength spectra. *J Geophys Res* 109:B06303, DOI 10.1029/ 2003JB002673.

Sens-Schönfelder, C., and U. Wegler (2006), Radiative transfer theory for estimation of the seismic moment, *Geophys. J. Int.*, 167(3), 1363–1372, doi:10.1111/j.1365-246X.2006.03139.x.

Shishov, V. L. (1974). Effect of refraction on scintillation characteristics and average pulsars, *Sov. Astron.* 17, 598–602.

Stevens, J. L., and S. M. Day (1985). The physical basis of the mb:Ms and variable frequency magnitude methods for earthquake/explosion discrimination, *J. Geophys. Res.* **90,** 3009–3020.

Tatarskii, V. I. (1971), The Effects of the Turbulent Atmosphere on Wave Propagation, *Isr. Program for Sci. Transl.*, Jerusalem.

Wegler, U., M. Korn, and J. Przybilla (2006), Modeling full seismogram envelopes using radiative transfer theory with born scattering coefficients, *Pure Appl. Geophys.*, 163(2–3), 503–531, doi:10.1007/s00024-005-0027-5.

Yoo, S.-H., J. Rhie, H. Choi, and K. Mayeda (2011), Coda-derived source parameters and their scaling relationships in the Korea Peninsula, *Bull. Seismol. Soc. Am*, 101(5), 2388-2398, doi:10.1785/0120100318.

Yoo, S.-H. (2017), Stable and Transportable Seismic Yield Estimation from Local Full Envelope Template Matching, Bull. Seismol. Soc. Am., 107, No. 2, doi: 10.1785/0120150148.

Yoshimoto K (2000), Monte-Carlo simulation of seismogram envelope in scattering media, *J. Geophys. Res*, 105:6153–6161, DOI 10.1029/1999JB900437.

Zhang, M., and Wen, L., (2014), Seismological evidence for a low-yield nuclear test on12 May 2010 in North Korea, *Seis. Res. Lett.*, 86, doi:10.1785/02201401170.

Zeng, Y. (1993), Theory of scattered P- and S-wave energy in a random isotropic scattering medium, *Bull. Seismol. Soc. Am.*, 83, 1264-1276.